THE ASTROPHYSICAL JOURNAL, 505:941–956, 1998 October 1

WAVELET ANALYSIS OF SOLAR FLARE HARD X-RAYS

MARKUS J. ASCHWANDEN[1]
Department of Astronomy, University of Maryland, College Park, MD 20742; markus@astro.umd.edu
BERNHARD KLIEM
Astrophysical Institute Potsdam, An der Sternwarte 16, D-14482 Potsdam, Germany
UDO SCHWARZ AND JÜRGEN KURTHS
Institut für Theoretische Physik und Astrophysik, Universität Potsdam, D-14469 Potsdam, Germany
AND
BRIAN R. DENNIS AND RICHARD A. SCHWARTZ
Laboratory for Astronomy and Solar Physics, Code 682, NASA/Goddard Space Flight Center, Greenbelt, MD 20771
Received 1998 February 18; accepted 1998 May 1

ABSTRACT

We apply a multiresolution analysis to hard X-ray (HXR) time profiles $f(t)$ of solar flares. This method is based on a wavelet transform (with triangle-shaped wavelets), which yields a dynamic decomposition of the power at different timescales T, the scalogram $P(T, t)$. For stationary processes, time-averaged power coefficients, the scalegram $S(T)$, can be calculated. We develop an algorithm to transform these (multiresolution) scalegrams $S(T)$ into a standard distribution function of physical timescales, $N(T)$. We analyze 647 solar flares observed with the *Compton Gamma Ray Observatory* (*CGRO*), recorded at energies ≥ 25 keV with a time resolution of 64 ms over 4 minutes in each flare. The main findings of our wavelet analysis are:

1. In strong flares, the shortest detected timescales are found in the range $T_{\rm min} \approx 0.1$–0.7 s. These minimum timescales are found to correlate with the flare loop size r (measured from *Yohkoh* images in 46 flares), according to the relation $T_{\rm min}(r) \approx 0.5(r/10^9$ cm) s. Moreover, these minimum timescales are subject to a cutoff, $T_{\rm min}(n_e) \gtrsim T_{\rm Defl}(n_e)$, which corresponds to the electron collisional deflection time at the loss-cone site of the flare loops (inferred from energy-dependent time delays in *CGRO* data).
2. In smoothly varying flares, the shortest detected timescales are found in the range $T_{\rm min} \approx 0.5$–5 s. Because these smoothly varying flares exhibit also large trap delays, the lack of detected fine structure is likely to be caused by the convolution with trapping times.
3. In weak flares, the shortest detected timescales cover a large range, $T_{\rm min} \approx 0.5$–50 s, mostly affected by Poisson noise.
4. The scalegrams $S(T)$ show a power-law behavior with slopes of $\beta_{\rm max} \approx 1.5$–$3.2$ (for strong flares) over the timescale range of $[T_{\rm min}, T_{\rm peak}]$. Dominant peaks in the timescale distribution $N(T)$ are found in the range $T_{\rm peak} \approx 0.5$–10^2 s, often coinciding with the upper cutoff of $N(T)$.

These observational results indicate that the fastest significant HXR time structures detected with wavelets (in strong flares) are related to physical parameters of propagation and collision processes. If the minimum timescale $T_{\rm min}$ is associated with an Alfvénic crossing time through elementary acceleration cells, we obtain sizes of $r_{\rm acc} \approx 75$–750 km, which have a scale-invariant ratio $r_{\rm acc}/r \approx 0.03$ to flare loops and are consistent with cell sizes inferred from the frequency bandwidth of decimetric millisecond spikes.

Subject headings: methods: statistical — Sun: flares — Sun: X-rays, gamma rays — waves

1. INTRODUCTION

Wavelet analysis allows a local decomposition of timescales in time series of transient nature or nonstationary processes. This is an important extension to Fourier analysis, which is designed to provide a global decomposition of time series with stationary properties. Wavelet analysis has been increasingly applied to astrophysical data sets, e.g., to study solar diameter variations (Vigoroux & Delache 1993), quasi-periodic oscillations in accretion disks (Scargle et al. 1993), the fine structure of the Encke gap ringlet (Bendjoya, Petit, & Spahn 1993), gamma-ray bursts (Young, Meredith, & Ryan 1995), solar magnetograms (Komm 1994, 1995), solar cycle variability (Watari 1995, 1996), solar chromospheric oscillations (Bocchialini & Baudin 1995), stellar chromospheric variations (Frick et al. 1997), weak source detection in *ROSAT* soft X-ray images (Damiani et al. 1997a, 1997b), solar helioseismology (Fröhlich et al. 1997), solar millimeter bursts (Schwarz et al. 1998), and other astrophysical applications (see Scargle 1993, and references therein). Here we attempt to investigate the timescales that govern solar flare hard X-ray (HXR) emission, which exhibits a challenging irregular temporal behavior that has never been successfully characterized by any time series method.

Extensive time series analysis of solar HXR data has been attempted with the Fourier method, but without revealing significant periodicities. Kiplinger et al. (1982) computed 2000 power spectra in 95 HXR flares observed with the Hard X-Ray Burst Spectrometer (HXRBS) (Orwig, Frost, & Dennis 1980) on board the *Solar Maximum Mission* (*SMM*) satellite, recorded with a time resolution of 128 ms at ener-

[1] Present address: Lockheed-Martin, Solar & Astrophysics Laboratory, Department H1-12, Building 252, 3251 Hanover Street, Palo Alto, CA 94304; aschwanden@sag.lmsal.com.

gies ≥ 25 keV, but found only three cases with marginal peaks in the Fourier power spectrum (at periods of $T = 0.17$, 0.39, and 0.81 s). Another search for periodicities, using HXR data from the more sensitive Burst and Transient Source Experiment (BATSE) (Fishman et al. 1989) on board the *Compton Gamma Ray Observatory* (*CGRO*), yielded a similar null result (M. E. Machado 1993, private communication). However, two preferred timescales were noticed by visual inspection of BATSE time profiles (Machado et al. 1993): (1) fast fluctuations on timescales of ≈ 0.1 s, and (2) large-amplitude fluctuations with timescales of ≈ 2–10 s, dubbed "elementary flare bursts" in earlier studies (De Jager & De Jonge 1978). Such large-amplitude fluctuations were found to be quasi-periodic sometimes (e.g., 16 s period, Parks & Winckler 1969; 8.2 s period in 1980 June 7 flare, Kiplinger et al. 1983b). A systematic analysis of timescales in BATSE HXR data was carried out by a numerical peak detection algorithm, using a 5 σ significance criterion in two energy channels (25 and 50 keV), yielding a total of 5430 HXR pulses from 181 different flares, which were characterized by an exponential distribution of timescales, $N(T) \exp \propto (-T/0.44\text{s})$ above a filter cutoff of $T > 0.3$ s (Aschwanden, Schwartz, & Alt 1995b). An obvious restriction of such a "sequential" pulse detection method is the lack of multiscale resolution, a capability that requires Fourier or wavelet methods.

While not much effort has been spent on time series analysis of HXR data of solar flares, there have been numerous methods applied to radio data. Because radio emission during solar flares is produced chiefly by nonthermal electrons as in HXRs, time structures of common electron acceleration and energy release processes are expected to show up in both wavelengths, as has been confirmed by numerous correlation studies (see, e.g., Dennis et al. 1984; Aschwanden, Benz, & Schwartz 1993; Aschwanden et al. 1995a). Time series analyses from radio data are therefore highly relevant to HXR data, although time structures of radio emission are probably convolved with timescales of the radiation process in a more complicated manner than for HXR bremsstrahlung radiation. Time series analyses of solar radio bursts include Fourier methods (Cliver et al. 1976; Mangeney & Pick 1989; Zhao, Mangeney, & Pick 1991), pulse interval statistics (Trottet et al. 1981; Aschwanden, Benz, & Montello 1994b), autocorrelation methods (Aschwanden et al. 1994a), correlation dimension or strange attractor dimension methods (Kurths & Herzel 1986, 1987; Kurths & Karlicky 1989; Kurths, Benz, & Aschwanden 1991; Isliker & Benz 1994; Ryabov et al. 1997), symbolic dynamics methods (Schwarz et al. 1993), and multiscale resolution or wavelet methods (Kurths, Schwarz, & Witt 1995; Schwarz et al. 1998).

In this paper we apply for the first time a wavelet analysis to HXR data of solar flares. We use a discrete wavelet algorithm (Bendjoya et al. 1993; Schwarz et al. 1998) that employs triangle-like wavelets, producing an output in form of scalograms $P(T, t)$ and time-averaged scalegrams $S(T)$. Because scalegrams represent the intrinsic timescales T in a convolved manner because of the multiresolution nature, we develop first a transformation that converts a scalegram $S(T)$ into a standard distribution function of physical timescales $N(T)$ (§ 2). We test the reliability of our transformation method by simulating surrogate data of time series $f(t)$ with predescribed distributions of timescales $N(T)^{\text{sim}}$, from which we calculate the scalegrams $S(T)$ and the inverted timescale distribution functions $N(T)^{\text{inv}}$ (§§ 3.1, 3.2, and 3.3). Further, we simulate test data with Poisson noise to study the sensitivity limit of the wavelet method on the shortest significant timescales (§ 3.4). In § 4 we present results from the wavelet analysis of the complete high–time resolution database from BATSE/*CGRO*, including 647 solar flares. We show scalegram examples from various flares, including the Masuda flare (§ 4.2), strong impulsive flares (§ 4.3), and slowly varying flares (§ 4.4). We explore the shortest significant time structures (§ 4.5) and relate them to the spatial sizes (§ 4.8) and electron densities of flare loops (§ 4.9). In § 5 we discuss some physical parameters and flare models in the context of wavelet timescales. A summary and conclusions are given in § 6.

2. WAVELET ANALYSIS METHOD

2.1. *Multiresolution Algorithm*

The wavelet transform can be considered as a generalization of the Windowed Fourier Transform, which yields a gliding power spectrum as function of time. The wavelet decomposition of a time series $f(t)$ yields information on the distribution of power at different temporal scales (an analog of the power spectrum) in every part of the time series. An orthogonal set of wavelet basis functions is derived from a "mother wavelet" $W(t)$ that satisfies the admissibility condition (see, e.g., Daubechies 1992; Meyer & Ryan 1993), which, in particular, implies that $\int_{-\infty}^{\infty} W(t)dt = 0$, if $W(t)$ is L^1 integrable. The wavelet functions are obtained by scaling a and translation b of the mother wavelet,

$$W_{a,b}(t) = C(a)W[a^{-1}(t-b)] , \tag{1}$$

where the normalization factor $C(a)$ is often chosen as $C(a) = |a|^{-1/2}$ to obtain an orthonormal basis. There exist unique decomposition and reconstruction formulas. Choosing $a = 2^j$ and $b = k\,\Delta t$, where Δt is the sampling interval of the signal $f(t)$, these formulas read

$$D_{j,k}(t) = \int_{-\infty}^{\infty} f(t)W_{j,k}(t)dt , \quad j, k \in Z , \tag{2}$$

and

$$f(t) = \sum_j \sum_k D_{j,k}\, W_{j,k}(t) , \tag{3}$$

where $D_{j,k}$ are the wavelet coefficients and Z is the set of integers.

Introducing a set of smoothing functions $q_{j,k}(t)$ enables efficient calculation of wavelet coefficients by recursion, often referred to as the discrete or pyramidal wavelet algorithm or multiresolution analysis (Mallat 1989). The $q_{j,k}(t)$ are again derived by scaling and translation of one function $q(t)$, which must be appropriately chosen to form an orthogonal basis in conjunction with the wavelet functions and to lead to convenient recursion formulas. In this paper we employ very compact wavelet and smoothing functions that enable analysis of time series down to the shortest scales—our main goal—and are necessarily coarse in the resolution of different timescales. These functions have already been used in Bendjoya et al. (1993) with emphasis on noise reduction and are given by

$$w(t) = \begin{cases} \dfrac{1}{2} - \dfrac{3|t|}{4\,\Delta t} & \text{for } \dfrac{|t|}{\Delta t} \leq 1 , \\ \dfrac{|t|}{4\,\Delta t} - \dfrac{1}{2} & \text{for } 1 < \dfrac{|t|}{\Delta t} \leq 2 , \\ 0 & \text{otherwise} , \end{cases} \tag{4}$$

$$q(t) = \begin{cases} \frac{1}{2} - \frac{|t|}{2\Delta t} & \text{for } \frac{|t|}{\Delta t} \le 1 , \\ 0 & \text{otherwise} , \end{cases} \quad (5)$$

$$w_k^j(t) = w[2^{-(j-1)}(t - k\,\Delta t)] , \quad j = 1, 2, \ldots , \quad k \in Z , \quad (6)$$

$$q_k^0 = 2q(t - k\,\Delta t) , \quad (7)$$

and

$$q_k^j(t) = q[2^{-j}(t - k\,\Delta t)] , \quad j = 1, 2, \ldots , \quad k \in Z . \quad (8)$$

The function $w(t)$ is sometimes called the triangle wavelet (see Fig. 1, *top panel*). In this algorithm, auxiliary coefficients at level $j = 0$ are first obtained from the data points $f_i = f(t_i) = f(i\,\Delta t)$, $i = 0, 1, 2, \ldots, N - 1$ according to

$$c_k^0 = \sum_i f(t_i) q_k^0(t_i) . \quad (9)$$

It can easily be seen that these coefficients are simply the data points themselves, $c_k^0 = f_k$, i.e., no smoothing has yet been performed and no contribution by wavelet coefficients is necessary to reconstruct the signal $f(t_i)$. The auxiliary coefficients at higher levels are computed by successively smoothing the time series at the corresponding scale:

$$c_k^j = \sum_i c_i^{j-1} q_k^j(t_i) , \quad j = 1, 2, \ldots , \quad (10)$$

where also the sampling increment increases by a factor of 2 between subsequent levels, i.e., the index i in the sum runs in steps of 2^{j-1}. A series of low-pass filters, whose width decreases by a factor of 2 between each level, is thus applied to the signal. Inserting equation (8) yields

$$c_k^j = \tfrac{1}{2} c_k^{j-1} + \tfrac{1}{4}(c_{k-2^{j-1}}^{j-1} + c_{k+2^{j-1}}^{j-1}) , \quad j = 1, 2, \ldots . \quad (11)$$

The wavelet coefficients that are derived from the smoothed time series (again with i running in steps of 2^{j-1}),

$$d_k^j = \sum_i c_i^{j-1} w_k^j(t_i) , \quad j = 1, 2, \ldots , \quad (12)$$

primarily contain contributions to the signal in the bandpass between levels $j - 1$ and j of the smoothing procedure. This becomes apparent also by evaluating the wavelet coefficients using equation (6):

$$d_k^j = c_k^{j-1} - c_k^j . \quad (13)$$

Equations (11) and (13) together with $c_k^0 = f_k$ constitute the recursion formulas used to calculate the wavelet coefficients d_k^j. At level j, mutually independent information about a scale $T_j = 2^j\,\Delta t$ exists on a sparse grid with spacing $2^{j+1}\,\Delta t$ only, but the recursion can be performed for any $k = 0, 1, 2, \ldots, N - 1$. It is meaningful at most up to a level $j < \log_2 N$. Close to the end points of the time series, the missing value in parentheses on the right-hand side of equation (11) is replaced by the end point c_0^{j-1} or c_{N-1}^{j-1}, respectively, so that the wavelet coefficients are inaccurate in an interval $\sum_{m=1}^{j} 2^{m-1}\,\Delta t = (2^j - 1)\,\Delta t$ at both ends. In the middle part of the time series, the reconstruction formula follows directly from equation (13) and $c_k^0 = f_k$:

$$f(t_k) = c_k^{j_{\max}} + \sum_{j=1}^{j_{\max}} d_k^j , \quad (14)$$

where $j_{\max}$ is the highest level included in the recursion.

The plot of the wavelet coefficients d_k^j as function of time t_k and (logarithmic) scale T_j is referred to as the scalogram, $P(t, T)$. Averaging the squares of the wavelet coefficients over (quasi-stationary) time intervals $[t_1, t_2]$ yields the scalegram,

$$S(T) = \langle\, |P(t, T)|^2 \rangle|_{t_1 < t < t_2} , \quad (15)$$

which represents in some sense the analog to the Fourier power spectral density $P(\nu)$ that is expressed as function of frequency $\nu = T^{-1}$. Examples of two-dimensional scalograms $P(t, T)$ and one-dimensional scalegrams $S(T)$, obtained from solar radio burst data, have been presented by Schwarz et al. (1998).

2.2. *Transformation of Scalegrams into Distribution Functions of Timescales*

Scalegrams $S(T)$ contain information on the distribution of timescales T of which the time profile $f(t)$ is composed. The scalegram can be considered as a convolution of the standard distribution function $N(T)$ of timescales T that are contained in $f(t)$. Here we introduce a kernel function $p(T)$ that describes this convolution and enables us to invert the timescale distribution $N(T)$ from a scalegram $S(T)$. This inversion is generally not unique, because the characterization of a time profile $f(t)$ by wavelet coefficients, as well as the superposition of multiple time structures per se, rep-

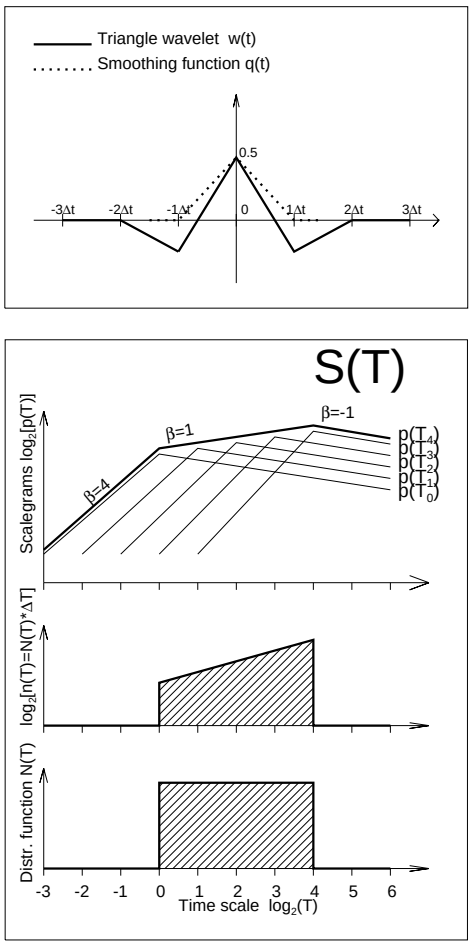

FIG. 1.—*Upper panel:* Triangle mother wavelet function $w(t)$ (*thick line*) and smoothing function $q(t)$ (*dotted line*). *Lower panel:* Schematic illustration of the convolution of a standard distribution function $N(T)$ (*bottom plot*) of timescales with kernel functions $p(T_i)$ (eq. [16]) that sum up to a scalegram $S(T)$.

resents an information loss. However, if there are single or dominant timescales T present in a time profile $f(t)$, the inversion with an appropriate kernel function $p(T)$ allows us to retrieve these dominant timescales T, which otherwise appear in the wavelet scalegrams $S(T)$ in a highly convoluted manner. It is important to note that the relationship between $N(T)$ and $S(T)$ will in general depend upon the choice of the wavelet algorithm, in particular on the chosen mother wavelet function. For a detailed theoretical study of scalegram properties as function of various elementary time profiles (e.g., triangles, rectangles, Gaussian profiles, etc.) we refer to a subsequent paper (Kliem et al. 1998).

Because time structures in solar flare HXRs generally exhibit Gaussian-like shapes (which can also be justified on a physical basis in terms of the logistic equation; Aschwanden, Dennis, & Benz 1998a), we employ the scalegram $S(T)$ of a Gaussian profile to infer the elementary kernel function $p(T)$. The scalegram $S(T)$ of a single Gaussian time profile $f(t)$ can be approximated by a double power law, having its steepest slope at small timescales ($\beta_1 \approx 4$), and a less steep negative slope at large timescales ($\beta_2 \approx -1$), i.e.,

$$p(T) = \begin{cases} (T/\tau)^4 & \text{for } T \le \tau \,, \\ (T/\tau)^{-1} & \text{for } T \ge \tau \,, \end{cases} \tag{16}$$

where τ is the characteristic timescale of the chosen elementary structure (the double FWHM for a Gaussian structure). This functional shape of $p(T)$ can also be calculated analytically (see Kliem et al. 1998).

Using the kernel function $p(T)$ defined in equation (16), we can write the functional form of a scalegram $S(T)$ as a superposition of all convolutions $p_j(T_i)$ of independent timescales T_i, i.e.,

$$S(T_j) = S_j = \sum_{i=1}^{n} n_i p_j(T_i) = \sum_{i=1}^{j} n_i \left(\frac{T_j}{T_i}\right)^{-1} + \sum_{i=j+1}^{n} n_i \left(\frac{T_j}{T_i}\right)^{4} . \tag{17}$$

This convolution can be written in form of a linear equation system, where the scalegram S_j is expressed by a matrix multiplication M_{ij} with the coefficients n_i,

$$S_j = n_i M_{ij} \,, \tag{18}$$

where the matrix M_{ij} has the numerical values

$$M_{ij} = \begin{pmatrix} 1 & 2^{-1} & 2^{-2} & 2^{-3} & \dots & 2^{-(n-1)} \\ 2^{-4} & 1 & 2^{-1} & 2^{-2} & \dots & 2^{-(n-2)} \\ 2^{-8} & 2^{-4} & 1 & 2^{-1} & \dots & 2^{-(n-3)} \\ 2^{-12} & 2^{-8} & 2^{-4} & 1 & \dots & 2^{-(n-4)} \\ \vdots & \vdots & \vdots & \vdots & \ddots & \vdots \\ 2^{-4(n-1)} & 2^{-4(n-2)} & 2^{-4(n-3)} & 2^{-4(n-4)} & \dots & 1 \end{pmatrix} . \tag{19}$$

The determination of the standard distribution of timescales $N(T)$ from a given scalegram $S(T)$ corresponds to the solution of this linear equation system (eq. [18]), which can be achieved by inverting the matrix M_{ij},

$$n_i = S_j M_{ji}^{-1} \,, \tag{20}$$

The inversion of matrix M specified in equation (19) yields

$$M_{ji}^{-1} = \begin{pmatrix} +1\frac{1}{31} & -\frac{2}{31} & 0 & 0 & \dots & 0 \\ -\frac{16}{31} & +1\frac{2}{31} & -\frac{2}{31} & 0 & \dots & 0 \\ 0 & -\frac{16}{31} & +1\frac{2}{31} & -\frac{2}{31} & \dots & 0 \\ 0 & 0 & -\frac{16}{31} & +1\frac{2}{31} & \dots & 0 \\ \vdots & \vdots & \vdots & \vdots & \ddots & \vdots \\ 0 & \dots & 0 & -\frac{16}{31} & +1\frac{2}{31} & -\frac{2}{31} \\ 0 & \dots & 0 & 0 & -\frac{16}{31} & +1\frac{1}{31} \end{pmatrix} , \tag{21}$$

which has the form of a tridiagonal matrix. The power coefficients $n_i = n(T_i)$ of the unconvolved timescale distribution can now directly be calculated from a scalegram $S_j = S(T_j)$ with equation (20) and the matrix M_{ji}^{-1} specified in equation (21).

Because the timescales $T_i = \Delta t \times 2^i$ of a scalegram are computed in steps by powers of 2, the bin widths ΔT_i are proportional to the timescales T_i, i.e.,

$$\Delta T_i = T_{i+1} - T_i = \Delta t (2^{i+1} - 2^i) = \Delta t \times 2^i = T_i \,. \tag{22}$$

In order to determine the distribution function $N(T)$ of timescales T, we have therefore to normalize the power $n_i(T_i)$ by the bin width ΔT_i, i.e.,

$$N(T_i) \propto \frac{n_i(T_i)}{\Delta T_i} = \frac{n_i(T_i)}{T_i} \,. \tag{23}$$

In summary, we derived an algorithm to back-transform a wavelet scalegram $S(T)$ into the timescale distribution $N(T)$, for the special case in which the time profile $f(t)$ consists of Gaussian functions. If the time profile consists of a single Gaussian function or a sequence of identical Gaussian functions, the back transformation should be fairly exact and render a δ-function of timescales, i.e., $N(T) = \delta(T - \tau)$. If the time profile $f(t)$ consists of a superposition of many Gaussian profiles with similar widths $T \approx \tau$, the inversion is expected to produce a peak in the timescale distribution $N(T)$ at $T \approx \tau$. If the time profile $f(t)$ consists of a superposition of a multitude of timescales, the inversion is not unique but should at least render the approximate range of timescales. We will demonstrate the accuracy of the inversion with examples in § 3.

We illustrate in Figure 1 the convolution of a timescale distribution function $N(T)$ with the kernel function $p(T)$. The scalegram $S(T_j)$ is composed of a sum of individual scalegrams $p_j(T_i)$ with power coefficients $n_i = N(T_i) \times T_i$. We visualize this convolution for the case of a distribution function that is constant, $N(T) = \text{const}$, over a range $T_1 < T < T_2$. The resulting scalegram $S(T)$ has a power-law slope β,

$$\beta(T) = \frac{\log_2 [S(T + \Delta T)] - \log_2 [S(T)]}{\log_2 (T + \Delta T) - \log_2 (T)} \,, \tag{24}$$

with a value of $\beta = 4$ at the shortest timescales $T < T_1$, a value of $\beta = -1$ at the largest timescales $T > T_1$, and an intermediate value of $\beta \approx 1$ in between (see Fig. 1, *middle panel*). The particular value of the slope in the intermediate time range depends also to some extent on the time intervals between the superimposed structures (see Kliem et al. 1998). Although the inversion of $N(T)$ is not unique, we expect with this method to retrieve dominant timescales, or

the approximate ranges of significant timescales in the distribution function $N(T)$.

3. WAVELET ANALYSIS OF SIMULATED DATA

The following numerical simulations serve the purpose to deepen our understanding of the employed wavelet code, especially: (1) how different temporal structures translate into a scalegram, (2) what information of the original time structure can be retrieved with our transformation into standard distribution functions of timescales, and (3) how accurately our inversion procedure renders the originally convolved timescales.

3.1. *Single Time Structures*

First we start with time series that contain only one single time structure, having the shape of a Gaussian profile, for which our inversion algorithm is optimized. We simulate time profiles $f(t)$ with Gaussian profiles of various widths τ, using a time resolution $\Delta t = 0.064$ s and a length of $N = 3776$ data points identical to the solar HXR data analyzed below. The time profile $f(t)$ of one case is shown in Figure 2 (*top left panel*; simulation A), for a Gaussian profile with a width of $\tau = 24.1$ s. The resulting scalegram (Fig. 2, *top middle panel*) exhibits a maximum slope with a power law of $\beta_{\max} = 3.79$, for timescales that are shorter than the

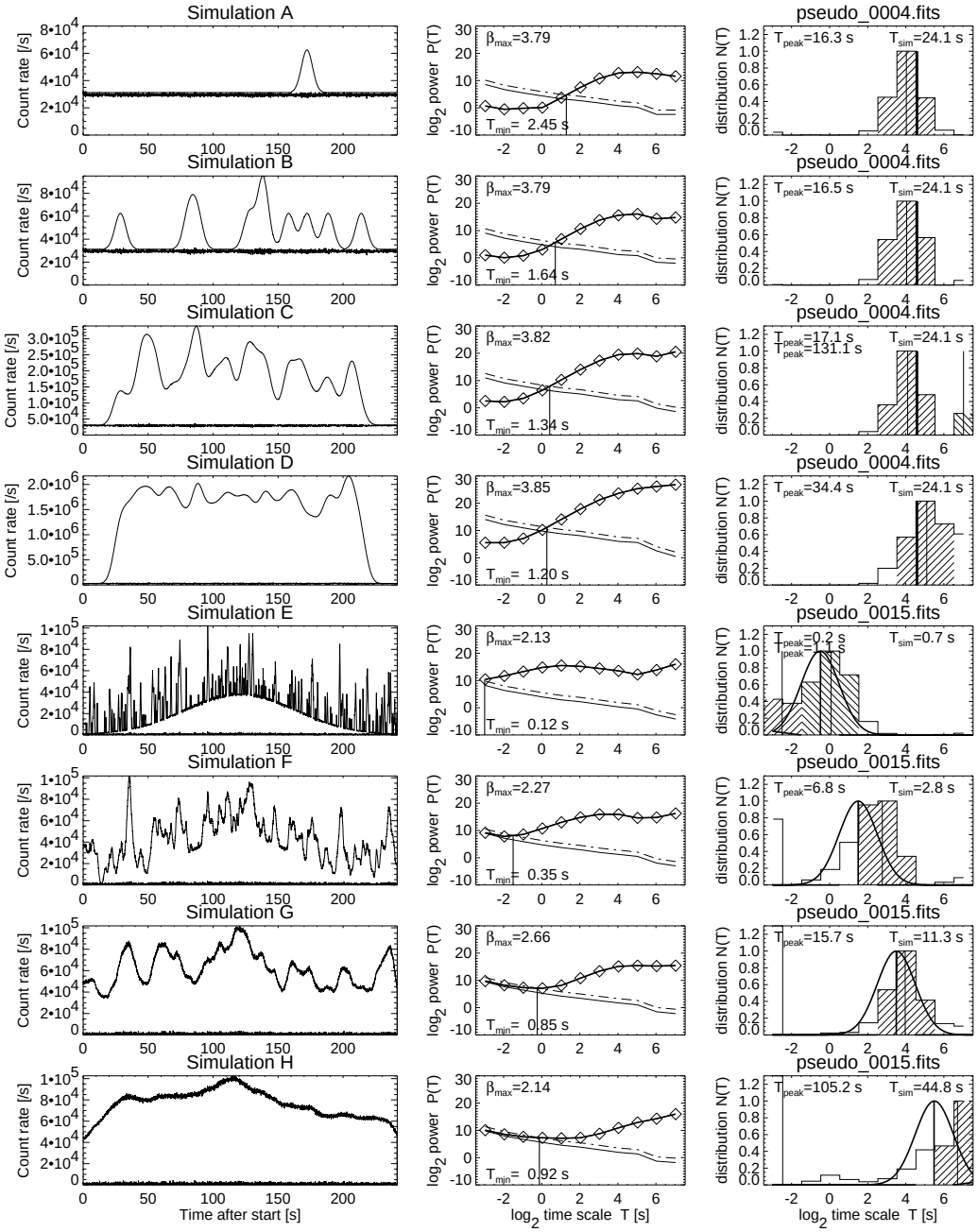

FIG. 2.—Eight numerical simulations (A–H) of time profiles $f(t)$ (*left panels*), the computed wavelet scalegrams $S(T)$ (*middle panels*), and the inverted timescale distribution functions $N(T)$ (*right panels*). The time profiles contain also the noise templates (*left panels*). The scalegrams (*middle panels*, *diamonds*) also contain the "noise scalegrams" (*thin solid lines*) with the 3 σ limit (*dashed lines*). The slope $\beta_{\max}$ is measured at the steepest part of the scalegrams. The inverted timescale distribution functions (*right panels*, *histograms*) are compared with the theoretical distribution functions (*thick lines*) used in the simulation of $f(t)$, with mean timescales $T_{\rm sim}$, and are compared with the inverted peak times $T_{\rm peak}$ (weighted over the hatched part of histogram).

Gaussian duration, $T < \tau$, and bends over to a slightly negative slope $\beta \approx -1$ for timescales that are longer than the Gaussian duration, $T > \tau$. Therefore, the scalegram of this single Gaussian profile reproduces closely the kernel function $p(T)$ defined in equation (16). Applying our transformation (eqs. [20], [21], [22], and [23]) yields a peaked distribution function $N(T)$ (Fig. 2, *top right panel*), with a peak value at a timescale of $T = 16.3$ s, and thus matches the Gaussian width ($\tau = 24.1$) to within a factor of 1.3. This is acceptable, given the coarse resolution of scalegrams by factors of 2. This test demonstrates the consistency of the inversion procedure for a singular time structure. We performed similar tests with triangular functions $f(t)$ and found an equally satisfactory inversion of triangle timescales.

Because peaks in timescale distributions $N(T)$ are often asymmetric, we define a weighted mean that includes also the adjacent bins to the peak (labeled with index i_p),

$$\log_2 (T_{\rm peak}) = \frac{\sum_{i=i_p-1}^{i_p+1} N_i \log_2 (T_i)}{\sum_{i=i_p-1}^{i_p+1} N_i} . \quad (25)$$

This notion is especially important in the next examples.

3.2. *Random Distributions of Time Structures*

Since wavelet analysis, unlike the Fourier Transform, provides local power decomposition in time, the degree of periodicity or randomness in the temporal arrangement of repeated time structures should not affect much the shape of a time-averaged scalegram. We expect therefore that the scalegrams of periodic or random sequences of identical Gaussian functions should be similar to that of a single Gaussian function. Consequently, our transformation of scalegrams into standard distribution functions $N(T)$ should also reveal the same δ-function $\delta(T - \tau)$ as for a single Gaussian function with duration τ.

We test this prediction with three simulations, labeled simulations B, C, and D in Figure 2. The time profiles $f(t)$ of these three cases were generated by superposition of 10, 10^2, or 10^3 identical Gaussian profiles with a duration of $\tau = 24.1$ s. The superposition of many structures leads to an erratic time profile where many elementary Gaussian profiles become unresolved. Despite of this confusion problem, the typical shape of elementary time structures still dominates the overall structure of the time profiles $f(t)$, and thus the wavelet decomposition produces scalegrams that are similar to that of a single Gaussian profile. Consequently, also the inverted distribution $N(T)$ reveals the same timescale of the convolved Gaussian time structure. For the three simulated cases, we retrieve the following values of the peak in the timescale distribution: $T_{\rm peak} = 16.5$, 17.1, and 34.4 s, which are all within a factor of $\lesssim 1.4$ of the elementary Gaussian duration, $\tau = 24.1$ s. We performed similar tests with periodic sequences of Gaussian structures and triangles. These tests confirm that elementary timescales can be retrieved from time-averaged scalegrams, regardless whether elementary time structures are fully or partially resolved, and irrespective of their degree of periodicity or randomness.

3.3. *Multiscale Distributions*

While we dealt with single-scale distributions in the previous simulations, we proceed now to the next level of complexity by introducing a finite width in the timescale distribution $N(T)$. In four simulations shown in Figure 2 (simulations E, F, G, and H), we employ a Gaussian distribution $N[\log_2 (T)]$ of logarithmic timescales, with a logarithmic width of $\sigma_T/\tau = 2$, centered around the timescales $\tau = 2^{-0.5+2*i}$, $i = 0, \ldots, 3$. The time profiles $f(t)$ are generated by superimposing 200 Gaussian functions with durations T defined by the Gaussian distribution function $N(T)$. In the wavelet analysis, we now obtain flatter slopes in the scalegrams, $\beta_{\rm max} = 2.13$, 2.27, 2.66, and 2.14, which are distinctly lower than those obtained for identical timescales ($\beta_{\rm max} = 3.79$–3.85 in simulations A–D) and thus indicate broader distributions of timescales according to our model of the convolution function (eq. [16]). The inverted distributions $N(T)^{\rm inv}$ of timescales have a width comparable to the simulated Gaussian distribution $N(T)$. The inferred timescales of the peaks in $N(T)$, $T_{\rm peak} = 1.1$, 6.8, 15.7, and 105.2 s, match the expected values of $\tau = 0.7$, 2.8, 11.3, and 44.8 s to within a factor of $\approx$2–3, comparable with the resolution of scalegrams. There is a bias toward longer timescales in some inverted timescale distributions, probably because of the clustering effect of closely spaced structures, an ambiguity that cannot be circumvented without a priori assumptions. From these and additional tests with other distributions $N(T)$, we conclude that our inversion procedure is capable of retrieving the peak timescale $T_{\rm peak}$ of an arbitrary distribution $N(T)$ to within an accuracy of a factor of $\lesssim 2$ in most cases.

3.4. *Poisson Noise*

The count rate of HXR photons obeys Poisson statistics. If N counts are recorded with a time resolution Δt, the count rate is defined by $C = N/\Delta t$, and the expected 1 σ fluctuation in the count rate due to Poisson statistics is

$$\sigma_N(t) \approx \sqrt{N(t)} = \sqrt{C(t)\,\Delta t} \quad (26)$$

in the approximation of $N \gg 1$. For *CGRO*/BATSE, the background is of order $C_{\rm backgr} \approx 3 \times 10^3$ counts s^{-1} for the first DISCSC channel (25–50 keV), while maximum count rates up to $C_{\rm max} \lesssim 2 \times 10^5$ counts s^{-1} are registered before instrumental saturation (pulse pile-up) occurs. For the high-resolution data used here ($\Delta t = 0.064$ s), the Poisson noise varies therefore between 7% for the weakest flares and 1% for the strongest flares.

The Poisson noise can dominate the shortest timescales in power spectra or in scalegrams $S(T)$ of wavelet analysis. In order to evaluate the minimum timescale $T_{\rm min}$ below which Poisson noise dominates time structures, we also compute for each analyzed flare time profile $C(t)$ the scalegrams of a corresponding Poisson noise template,

$$C_{\rm noise}(t) = \rho(t)\sigma_C(t) = \rho(t)\,\frac{\sigma_N(t)}{\Delta t} = \rho(t)\sqrt{\frac{C(t)}{\Delta t}} , \quad (27)$$

where $\rho(t)$ represents a random number for each time bin $t_i = i\,\Delta t$, drawn from a Poissonian random distribution with a standard deviation of $\sigma_\rho = 1$. From this noise template $C_{\rm noise}(t)$, we calculate the scalegrams $P_{\rm noise}(T)$. Comparing these "noise scalegrams" $P_{\rm noise}(T)$ with the scalegrams $S(T)$ of flare data, we consider significant only those time structures that have timescales in which the scalegram exceeds the "noise scalegram" by a factor of 3 σ (corresponding to a signal-to-noise ratio of > 3), i.e.,

$$\frac{S(T > T_{\rm min})}{S_{\rm noise}(T > T_{\rm min})} \geq 3 , \quad (28)$$

defining a criterion for the minimum timescale $T_{\rm min}$, above which time structures are significant. A similar technique was used by Scargle et al. (1993), who subtracted the "noise scalegram" to obtain a "noise-corrected" scalegram, i.e., $S_{\rm corr}(T) = S(T) - S_{\rm noise}(T)$.

The influence of Poisson noise on the range of significant timescales $T > T_{\rm min}$ in the scalegram $S(T)$ is illustrated in Figure 3. For an arbitrary (smoothed) flare time profile with a count rate of $C = 2 \times 10^5$ counts s^{-1}, we find a minimum timescale of $T_{\rm min} = 0.99$ s (Fig. 3, *top row*). If we scale the flux of the same time profile by factors of 0.1 and 0.01, the minimum timescale increases to values of $T_{\rm min} = 2.07$ and 4.74 s, respectively (Fig. 3, *second and third rows*). If we generate pure Poisson noise (from a random generator), the scalegram does not show any significant structure up to $T_{\rm min} > 38.93$ s (Fig. 3, *bottom row*). The inverted timescale distribution $N(T)$ shows a peak for the shortest unresolved structures $T \leq 0.128$ s.

From the simulations in Figure 3, we see also that the steepest slope of the scalegram systematically drops from a value of $\beta_{\rm max} = 2.46$ at high count rates (Fig. 3, *top row*) to $\beta_{\rm max} \approx 0.38$ at the Poisson noise level. The latter scalegram is consistent with a white noise spectrum or $1/f$-noise processes. To visualize the Poisson noise limit in scalegrams, we display also the "noise scalegram" $P_{\rm noise}(T)$ in all figures. In these scalegrams, it can clearly be seen that the scalegram $S(T)$ of real data always shows a steeper slope for significant timescales $T > T_{\rm min}$ than the "noise scalegram" $P_{\rm noise}(T)$. Note that flatter slopes have also been observed for the radio noise of the quiet Sun ($\beta = 1.37 \pm 0.59$) and the sky ($\beta = 1.03 \pm 0.96$) in Schwarz et al. (1998).

4. WAVELET ANALYSIS OF OBSERVED DATA

4.1. *Data Set*

For our wavelet analysis of solar hard X-ray (HXR) data, we require a high signal-to-noise ratio and a large dynamic range of timescales. These criteria are best satisfied with data from the Burst and Transient Source Experiment (BATSE) (Fishman et al. 1989) on board the *CGRO* spacecraft. The eight large-area detectors (LADs), with a collecting area of 2000 cm^2 each, are the most sensitive HXR detectors ever flown and thus have (despite of the higher background count rate) a higher signal-to-noise ratio than other HXR detectors used for solar flare observations (e.g., *Hinotori*, *SMM*/HXRBS, or *Yohkoh*/HXT, with typical collecting areas of ≈ 70 cm^2). From the BATSE archive, we select the DISCSC burst trigger data, which have a uniform time resolution of 64 ms over a duration of 4 minutes and thus provide a dynamic range of $T_{\rm max}/T_{\rm min} = 241.664$ s/0.064 s $= 3776 \approx 2^{12}$ for timescale analysis. We restrict our wavelet analysis to the lowest of the 4 DISCSC energy channels, 25–50 keV, which has the most counts per channel. The DISCSC data set contains 647 (analyzable) solar flare events during the years 1991–1995. We analyze the full data set in order to obtain representative results.

4.2. *Example of an Analyzed Flare*

As an example, we show a two-dimensional scalogram $P(T, t)$ for the most prominent flare of our data set, the Masuda flare on 1992 January 13, 1727 UT (Fig. 4). This flare is known for the discovery of above-the-loop-top HXR sources (Masuda 1994) and has been extensively analyzed (Masuda et al. 1994, 1995; Takakura et al. 1993; Hudson 1994; Hudson & Ryan 1995; Wang et al. 1995; Doschek, Strong, & Tsuneta 1995; Wheatland & Melrose 1995; Tsuneta 1995, 1996; Shibata et al. 1995; Aschwanden et al. 1996a; Alexander & Metcalf 1997). The HXR time profile of the 25–50 keV HXR flux is shown along with the noise template (eq. [27]) in the top panel of Figure 4. The two-dimensional scalogram $P(T, t)$ is shown in the middle panel of Figure 4, in which the gray scale renders the logarithmic power of the 11 timescales between 0.128 s and 131.072 s as

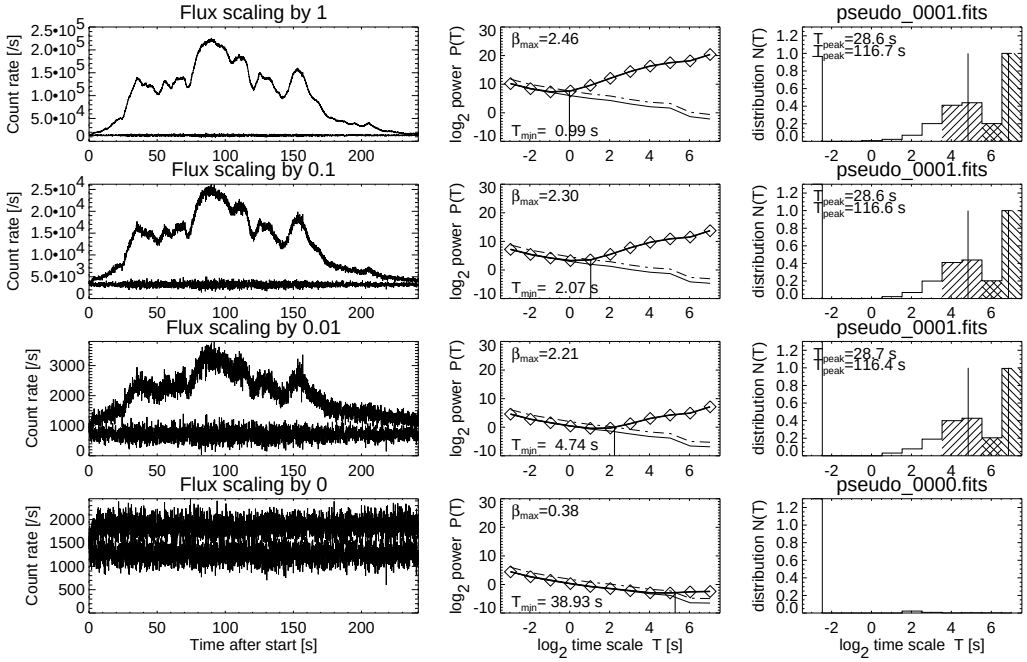

FIG. 3.—(Slightly averaged) time profile (*top row*) taken from the flare 1991 May 31, 1653:15 UT, is scaled down by factors of 0.1 (*second row*) and 0.01 (*third row*), with adjusted Poisson noise, to demonstrate the increase of the minimum significant timescale $T_{\rm min}$ (indicated at bottom of scalegrams in middle panels). The time profile in the bottom row shows pure Poisson noise, for which no significant timescale is found up to $T_{\rm min} > 39$ s with the 3 σ significance criterion (eq. [28]).

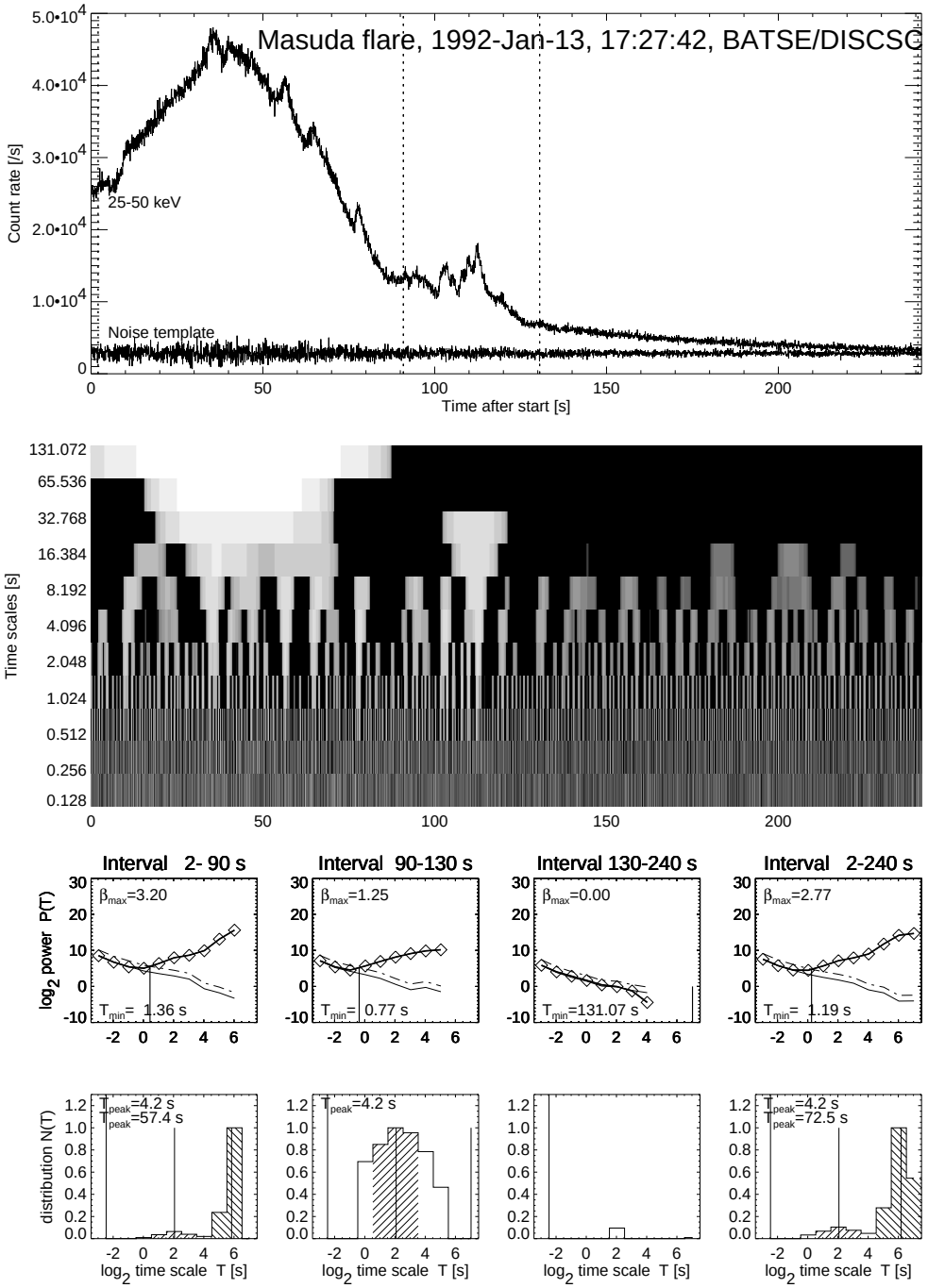

FIG. 4.—Time profile (*top panel*), scalogram $P(T, t)$ (*middle panel* with gray scale), time-averaged scalegrams $S(T)$ (*third row*), and inverted timescale distribution functions $N(T)$ (*fourth row*) for the Masuda flare, 1992 January 13, 1727:42 UT, observed with BATSE/*CGRO*.

function of time. We show time-averaged scalegrams for three subsequent time intervals (2–90 s, 90–130 s, and 130–240 s), and for the total flare interval (2–240 s) in the third row of Figure 4. Note that the maximum slope of the scalegram is high during the impulsive phase ($\beta_{\max} = 1.25$–3.20), but drops to the white-noise level after the flare ($\beta_{\max} \lesssim 0$). Averaging the entire flare yields still a value ($\beta_{\max} = 2.77$) that is typical for the most impulsive part, because the quiet interval after the flare has only a negligible contribution in the averaging of power coefficients. The selection of the analyzed time interval is therefore not critical, because the average is always dominated by the most structure-rich episodes. Investigating the shortest significant time structures, we find that the minimum timescales vary from $T_{\min} = 1.36$ s during the weakly modulated flare peak ($t = 2$–90 s) to $T_{\min} = 0.77$ s during the stronger modulated decay phase ($t = 90$–130 s) and indicate no structures up to $T_{\min} > 131$ s after the flare ($t = 130$–240 s). The inverted timescale distributions $N(T)^{\rm inv}$ (Fig. 4, *bottom row*) show during the main flare peak ($t = 2$–90 s) the most dominant structure at $T_{\rm peak} = 57.4$ s and a secondary dominant structure at $T_{\rm peak} = 4.2$ s. The latter timescale, $T_{\rm peak} = 4.2$ s, becomes dominant in the decay phase ($t = 90$–130 s), revealing a broad distribution $N(T)$ of timescales, extending over an approximate range of $1 \lesssim T \lesssim 32$ s. This example demonstrates that the distribution function of physical timescales

$N(T)$ is clearly peaked, a characteristic that is not immediately evident from the scalegram $S(T)$.

4.3. *Examples of Strong Impulsive Flares*

In Figure 5, we show eight examples of strong flares with count rates of $C \gtrsim 10^5$ counts s^{-1}, which have an excellent signal-to-noise ratio and should thus reveal the timescales of the shortest detected time structures. These eight events represent the largest *CGRO* flares (recorded with high time resolution) that have been simultaneously observed with *Yohkoh*; they are also analyzed in Aschwanden et al. (1996c, and references therein). The scalegrams of these eight flares all exhibit high values for the maximum slope, $\beta_{\max} = 1.53$–2.87 (Fig. 5, *middle column*). Short dominant timescales of $T_{\rm peak} = 1.0$–6.1 are found in four flares, while the longer dominant timescales in the range $T_{\rm peak} \approx 20$–90 s are typical for the duration of the flare or the main peak. However, significant time structures are found down to $T_{\min} = 0.128$–0.58 s for these eight flares. It is interesting to note that the autocorrelation width of filtered pulses analyzed in Aschwanden et al. (1996b) has intermediate values $w_{\rm AC} = 0.4$–1.6 s, between the fastest significant ($T_{\min}$) and dominant ($T_{\rm peak}$) time structures identified here.

An exceptional case among these eight flares is the last one (1992 February 14, 2306 UT), which shows no dominant time structure up to $T_{\rm peak} = 76$ s. The time profile shows almost no modulation depth. A deconvolution of this time profile into a directly and trap-precipitating component revealed an unusually high trapping ratio of $q_{\rm Trap} = (1 - q_{\rm prec}) = 0.8 \pm 0.1$ (Table 1 in Aschwanden, Schwartz, & Dennis 1998b). Because trapping represents a convolution of the electron injection profile pulses with a

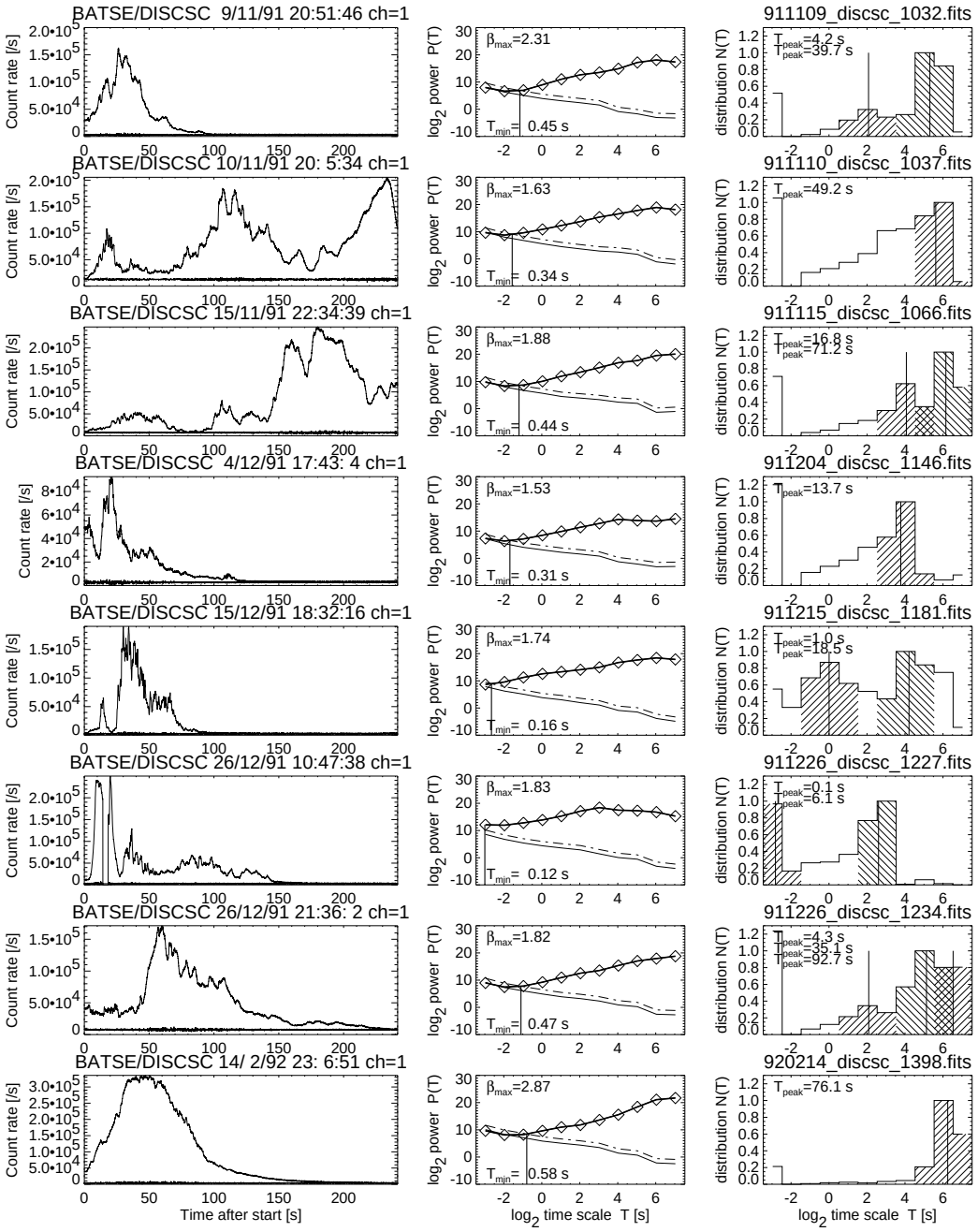

FIG. 5.—Time profiles (*left panels*), scalegrams (*middle panels*), and inverted timescale distribution functions $N(T)$ (*right panels*) for the eight strongest flares simultaneously observed with *CGRO* and *Yohkoh* (Aschwanden et al. 1996c). Representation similar to Fig. 2.

usually longer trapping timescale, the high trapping efficiency measured for this particular flare explains the lack of fast time structures, and thus the lack of a dominant short timescale. Consequently, because of the occasionally substantial contamination by trapped particles, information on intrinsic timescales of electron injection or acceleration processes can be heavily masked in the signal $f(t)$, and hence also in the scalegrams $S(T)$ and the inverted distribution functions $N(T)$.

4.4. *Examples of Smoothly Varying Flares*

The occasional lack of detected fine structure is most evident in a subset of flares (See Fig. 6) that was selected by the criterion of large energy-dependent time delays for high-energy electrons. This subset of five flares, where the largest negative delays were measured, i.e., $\tau = t_{25}$ keV $- t_{50}$ keV $= -2.3, \ldots, -7.6$ s, is also analyzed in Figures 7 and 8 of Aschwanden & Schwartz (1995). Because these time delays were found to be consistent with the energy-dependent timing of trapped electrons in terms of collisional deflection times $[t^{\rm Defl} \propto (E)E^{3/2}/n_e]$, these flares were interpreted in terms of high trapping efficiencies (Aschwanden & Schwartz 1995). Because of the relatively long trapping times ($\approx$2–7 s), all shorter time structures of the injection function are smoothed out, leading to a smoothly varying time profile for the observed HXRs. Consistent with this interpretation, we find minimum timescales of $T_{\rm min} = 2.35$–5.81 s from the scalegrams with our wavelet analysis, indicating that there are no shorter time structures present in the data, although the count rate is sufficiently high to allow for detection of subsecond structures at fairly low modulation depths (say $\gtrsim$3%; see Fig. 7). These examples clearly demonstrate that the shortest detected time structures $T_{\rm min}$ are sometimes related to physical processes rather than to the significance limit of Poisson noise, as is usually the case for weak flares.

4.5. *The Shortest Significant Time Structures*

The timescale diagnostics of wavelet analysis extends down to a limit of twice the data time resolution, here $T \geq 2 \times \Delta t = 0.128$ s, because the smallest resolved structures extend over two sampling intervals. On the other side, the Poisson noise of the HXR photon count statistics imposes fluctuations $\sigma_N = (CT)^{1/2}$ (eq. [26]) during a time interval T. Considering a fine structure with count rate C_q, which we characterize with a modulation depth $q = (C_q - C)/C$ with respect to the "local background" count rate C, the significance n_σ in units of the rms noise is

$$n_\sigma = \frac{N_q}{\sigma_N} = \frac{(C_q - C)T}{\sqrt{CT}} = q\sqrt{CT}\ . \tag{29}$$

From this criterion we can specify the shortest significant timescale $T_{\rm sign}$ with a significance of n_σ (e.g., $n_\sigma > 3$) as function of the count rate C and modulation depth q:

$$T_{\rm sign} = \left(\frac{n_\sigma}{q}\right)^2 \frac{1}{C}\ . \tag{30}$$

These shortest significant timescales $T_{\rm sign}$ are shown in Figure 7 (*left panel*, *dashed lines*) as function of the count rate C, for $n_\sigma \geq 3$ and different modulation depths $q = 0.1$, 0.03, and 0.01.

On the other hand, we measured the minimum significant timescales $T_{\rm min}$ of 647 solar flares from the "noise

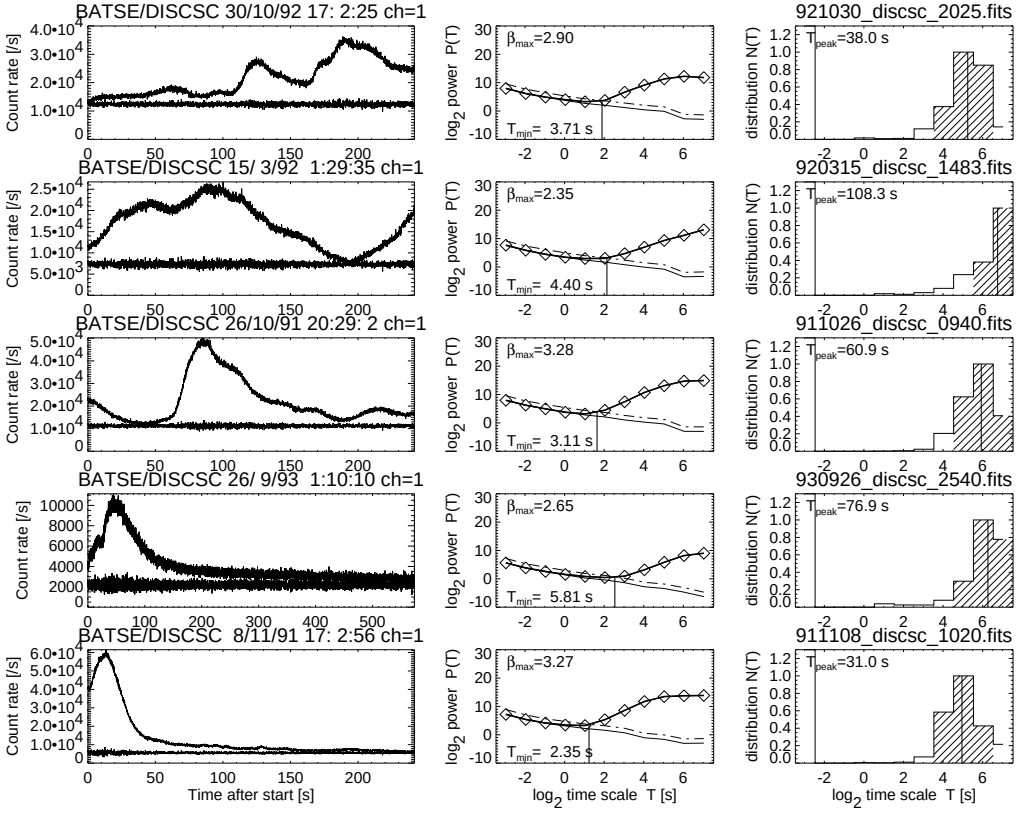

FIG. 6.—Time profiles (*left panels*), scalegrams (*middle panels*), and inverted timescale distribution functions $N(T)$ (*right panels*) for five smoothly varying flares with the largest observed trap delays (Aschwanden & Schwartz 1995). Representation similar to Fig. 5.

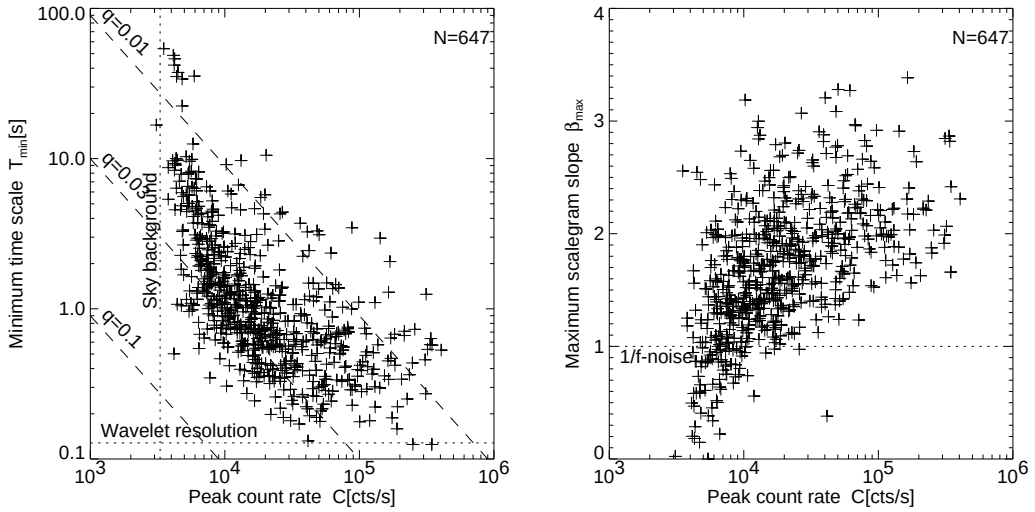

FIG. 7.—Scatter plot of the minimum timescale T_{min} vs. the peak count rate C (*left panel*), and of the maximum (scalegram) power-law slope β_{max} vs. peak count rate C (*right panel*), measured from 647 *CGRO* flares. The 3 σ significance limits for three different modulations depths ($q = 0.01$, 0.03, and 0.1) as defined in eq. (30) are indicated with dashed lines (*left panel*).

scalegrams" $P_{noise}(T)$ with criterion equation (28) (as illustrated in Fig. 3). These observed minimum timescales are plotted with cross symbols in Figure 7 (*left panel*). The theoretical curves $T_{sign}(C, q = \text{const}, n_\sigma = 3)$ (eq. [30]) shown in Figure 7 yield a lower limit of the modulation depth q for a structure to be detected at a significant level. The lack of detected significant structures on timescales $T(C) < T_{min}(C)$ in our scalegrams is, however, not always caused by Poisson noise but could also indicate the absence of physical processes on such short timescales as $T < T_{min}$.

4.6. *Distribution of Minimum and Peak Timescales*

From our wavelet analysis, we determined two kinds of timescales for each of the 647 flares: (1) the minimum timescale T_{min}, which represents the shortest significant detected time structures, and (2) the peak times T_{peak} of the inverted distribution function $N(T)$. In the case of multiple peak timescales T_{peak}, we refer to only the shorter one in the following. The distributions and a scatter plot of the two timescales T_{min} and T_{peak} are shown in Figure 8. Both distributions of timescales T_{peak} extend down to the wavelet resolution $\Delta T = 0.128$ s. The distribution of peak times T_{peak} can be characterized with a power law $N(T_{peak}) \propto T_{peak}^{-0.73}$ over a limited range, 8s $\leq T_{peak} \leq$ 64 s, or with an exponential distribution $N(T_{peak}) \propto \exp(-T/34.6\text{ s})$ over a larger range, at least 0.5–64 s (Fig. 8, *bottom panel*). The distribution of minimum timescales T_{min} has much lower values and can be characterized with an approximate power law of $N(T_{min}) \propto T_{min}^{-0.70}$ in a limited range, 0.5 s $< T_{min} <$ 4 s, or with an exponential distribution $N(T_{peak}) \propto \exp(-T/2.8\text{s})$ over a larger range (Fig. 8, *middle panel*). In comparison, the distribution of 5430 pulse durations measured in Aschwanden et al. (1995b) was characterized with an exponential distribution $N(T_P) \propto \exp(-T_P/0.44\text{ s})$, over a similar timescale range (0.3 s $< T_P <$ 2 s). There is no obvious correlation between the two timescales T_{min} and T_{peak} (see Fig. 8, *top panel*). The range of timescales $T_{min} < T < T_{peak}$ represents for each flare a continuous distribution of detected timescales, with a concentration of the spectral power at the timescale T_{peak}.

4.7. *Slope of Scalegrams*

Because the power-law slope β (eq. [24]) of scalegrams $S(T)$ was used in earlier work to characterize the scaling behavior in different events, we show this quantity for all 647 analyzed flares in Figure 7 (*right panel*), as function of the count rate C. Because this slope varies as function of the timescale T, we show the maximum values β_{max}, which tend to arise at the smallest scales above the noise limit T_{min}. From Figure 7 we note several properties: (1) the slope β_{max} is always steeper than the slope expected for white noise ($\beta \gtrsim -1$) (2) but never exceeds the theoretically predicted upper limit of $\beta \leq 4$, and (3) the slope is steepest ($\beta_{max} \approx$ 1.5–3.2) for strong flares ($C \gtrsim 10^5$ counts s^{-1}) and (4) picks up systematically lower values ($\beta_{max} \approx$ 0.0–2.5) for weaker flares ($C \lesssim 10^4$ counts s^{-1}). The latter effect is clearly produced by the increased Poisson noise contamination at shorter timescales for weak flares. Consequently, we should concentrate on the strongest flares to investigate the inherent distribution of physical timescales.

The scalegram slopes of the strongest HXR flares, $\beta_{max} \approx$ 1.5–3.2, are found to be compatible with those reported for solar radio bursts at millimeter wavelengths, with $\beta \approx$ 2.2–2.7 during the main flare phase. The latter were brought into context with the physical process of fractional Brownian motion, which was realized with a scalegram slope of $\beta = 2.25$ (Schwarz et al. 1998).

4.8. *Minimum Timescales and Flare Loop Sizes*

For a subset of 46 events of the 647 analyzed *CGRO* flares, the flare loop geometry was determined from images of the *Yohkoh* Soft X-Ray Telescope (SXT) and Hard X-Ray Telescope (HXT) in a study by Aschwanden et al. (1996b). The curvature radii r of the flare loops were measured from the footpoint separation of the magnetically conjugate HXR footpoint sources, after loop identification with SXT and correction for geometric projection effects. This sample of flare loops was found to have radii in the range $r =$ 3,000–25,000 km, and a scaling law between the loop half-length $s = r(\pi/2)$ and the electron time-of-flight dis-

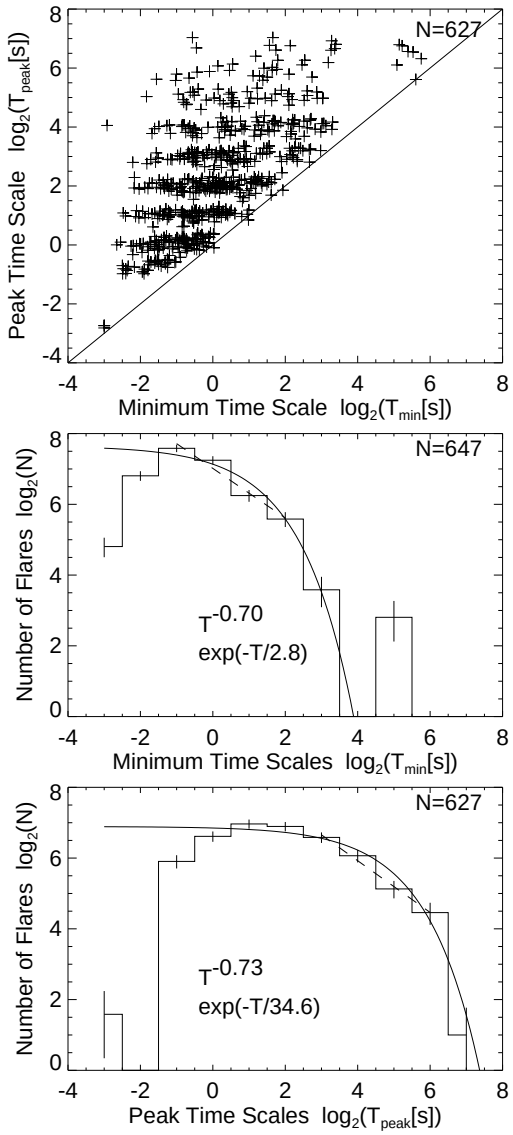

FIG. 8.—Distribution of peak timescales $N(T_{peak})$ (*bottom panel*) and minimum timescales $N(T_{min})$ (*middle panel*), and scatter plot of the two timescales (*top panel*). Note that there is no correlation between the two timescales.

tance l_{TOF} was discovered: i.e., $l_{TOF}/s = 1.4 \pm 0.3$ (Aschwanden et al. 1996b).

We show a scatter plot of the flare loop radii r, determined by spatial images from *Yohkoh*, and the minimum timescales T_{min}, measured with our wavelet analysis from *CGRO* data for this subset of 46 flares in Figure 9 (*left panel*). The minimum timescales T_{min} are bound by a lower limit of 0.128 s because of the wavelet resolution and are distributed mostly in the range $T_{min} \approx 0.1$–0.7 s. In Figure 9 we mark each of the 46 flares with a symbol whose magnitude is proportional to the (logarithmic) peak count rate of the flare. The scatter plot in Figure 9 (*left panel*) reveals a systematic correlation between the shortest detected timescales T_{min} and the flare loop size r. The functional relation is approximately linear, with a ratio that has the following mean and standard deviation for the range $T_{min} < 0.9$ s,

$$T_{min} = 0.49 \pm 0.28 \left(\frac{r}{10^9 \text{ cm}} \right) \text{ s} . \quad (31)$$

This relation seems not to be affected by sensitivity limitations due to Poisson noise, because the peak count rate C is not correlated with the loop size r. Only large values of the minimum timescale $T_{min} \gtrsim 0.9$ s are more likely to belong to weaker flares, where Poisson noise probably affects the shortest detected significant timescales (see also Fig. 7).

4.9. *Minimum Timescales and Flare Loop Densities*

For the same subset of flares we correlate the minimum timescale T_{min} with the electron density n_e, determined in 34 flares from the collisional deflection time $t^{Defl} \propto (E)E^{3/2}/n_e$ that was fitted to energy-dependent time delays of the HXR trap component (Aschwanden et al. 1996b). These electron densities were found in a range $n_e \approx 10^{10}$–2×10^{12} cm^{-3}. High densities $n_e \gtrsim 10^{12}$ cm^{-3} may have a systematic uncertainty toward too high values, because they are based on the separation of two small but competing delays. However, the lower density values $n_e \lesssim 10^{11}$ cm^{-3} have relatively small uncertainties (see Aschwanden et al. 1996b).

The minimum timescales T_{min} detected in wavelet scalegrams here are found to be systematically longer for low electron densities than for high densities (Fig. 9, *right panel*) and thus appear to be correlated with the electron density in a reciprocal way. This trend is most pronounced for the smallest minimum timescales $T_{min}(n_e)$ detected at each density n_e, forming a sharp cutoff. This sharp cutoff applies to flares with medium to high peak count rates (large symbols in Fig. 9, *right panel*) and is thus not affected by Poisson noise. In § 5 we discuss how this cutoff relates to collisional timescales.

5. DISCUSSION

The wavelet analysis has revealed two different timescales, the minimum timescale T_{min} and the peak timescale T_{peak}. In the following we discuss the possible meaning of these timescales in terms of some physical parameters that are likely to play roles in the flare process.

5.1. *The Spatio-Temporal Correlation*

The main result of this study is the discovery of the two correlations $T_{min}(r)$ and $T_{min}(n_e)$ for the minimum timescale found in wavelet scalegrams. The correlation between these three physical parameters was obtained from two completely independent data sets. While the minimum timescale T_{min} was measured from *CGRO* time profiles, and the electron density n_e from energy-dependent time delays in *CGRO* dynamic spectra, the flare loop (curvature) radii r have been measured from *Yohkoh*/HXT and SXT images. The parameters r and n_e, however, are largely uncorrelated, and therefore appear to be independent. It is not clear how the two correlations $T_{min}(r)$ and $T_{min}(n_e)$ can be combined into a single functional relation $T_{min}(r, n_e)$ without applying a specific physical flare model.

The correlation $T_{min} \propto r$ indicates an approximately constant ratio between a spatial and temporal scale, which has the physical dimension of a velocity. The proportionality constant could therefore be related to a characteristic velocity that does not depend on the size of the flare loop, e.g., (1) the speed of light c, (2) a particle propagation speed v_p, (3) an Alfvénic propagation speed v_A, or (4) a shock wave propagation speed. If the timescale T_{min} corresponds to a propagation time T_{prop} over a distance l with an approximately constant velocity v, this distance $l = qr$ has necessarily to

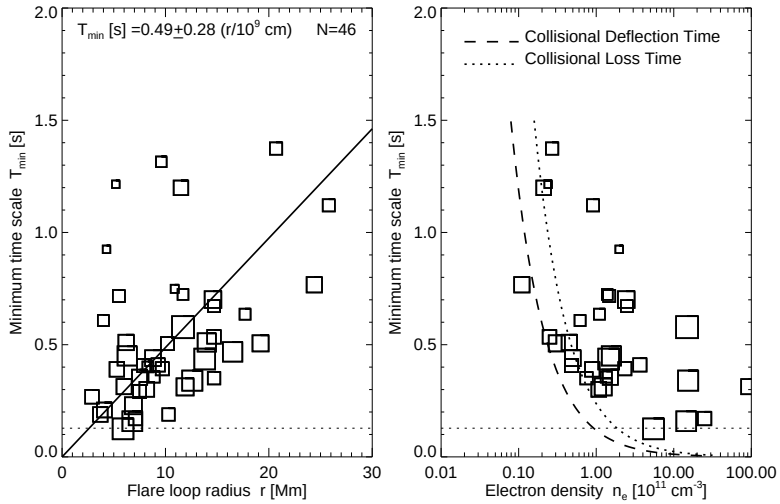

FIG. 9.—Correlation of the minimum timescale $T_{\min}$ with the flare loop radius r (*left panel*) and trap electron density n_e (*right panel*) for a subset of 46 flares simultaneously observed with *CGRO* and *Yohkoh* (Aschwanden et al. 1996b). The symbol size of the data points is proportional to the logarithm of the count rate. The mean ratio $T_{\min}/r$ (eq. [31]) is indicated (*left panel*, *solid line*), and collisional timescales for 25 keV electrons are shown (*right panel*, *dashed* and *dotted lines*).

scale with the flare loop size r, in order to be consistent with the correlation $T_{\min} \propto r$,

$$T_{\rm prop} = \frac{l}{v} = \frac{qr}{v} \,. \tag{32}$$

For a given velocity v, we then obtain the relative size $q = l/r$ of the propagation distance l (in units of flare loop radii r) from our correlation (eq. [31]) by setting $T_{\rm prop} = T_{\min}$, i.e.,

$$q = v\,\frac{T_{\rm prop}}{r} = v\,\frac{T_{\min}}{r} \approx 0.5\left(\frac{v}{10^9\ {\rm cm\ s^{-1}}}\right). \tag{33}$$

1. *Electromagnetic Propagation.*—It is unlikely that $T_{\min}$ is associated with a light travel speed $v = c = 3 \times 10^{10}$ cm s^{-1} because the required propagation distances would be a factor of $q = 0.5(c/10^9\ {\rm cm\ s^{-1}}) = 15$ times larger than the flare loops.

2. *Particle Propagation.*—Electron propagation distances also seem to be too large. If we consider 25–50 keV electrons ($v_e = 0.3$–$0.4c$), which contribute most to the observed $\geq$25 keV HXR emission to which the wavelet analysis is applied, we obtain a distance ratio that is $q = l/r = 4.5$–6 times larger than the flare loop radius. For comparison, the average electron time-of-flight distance was inferred to be a factor of 2–3 smaller from the analysis of HXR pulse delays, namely $l_{\rm TOF}/r = (\pi/2)*1.4 \pm 0.3 = 2.2 \pm 0.5$ (Aschwanden et al. 1996b).

3. *Alfvénic* Propagation.—If we consider the propagation time of an Alfvénic disturbance (with velocity $v_{\rm A}$) through a spatial structure with size $l = qr$, we obtain from the definition of the Alfvén velocity $v_{\rm A} = 2.18 \times 10^6 B\,[{\rm G}]/(n_e[{\rm cm^{-3}}])^{1/2}$,

$$q = 0.5\left(\frac{v_{\rm A}}{10^9\ {\rm cm\ s^{-1}}}\right) = 0.034\left(\frac{B}{100\ {\rm G}}\right)\left(\frac{n_e}{10^{11}\ {\rm cm^{-3}}}\right)^{-1/2}. \tag{34}$$

Such small spatial scales of only $\approx$3% of the flare loop radius, which correspond to distances of $l = 75$–750 km in our sample of flares (with $r = 2.5$–25 Mm), could possibly be associated with the sizes of elementary acceleration cells. Subsecond timescales $T_{\min} \approx 0.1$–0.7 observed in HXRs have traditionally been associated with elementary spatial cells of a fragmented energy release region (see, e.g., Kiplinger et al. 1983a; Emslie 1983; Machado et al. 1993; LaRosa & Moore 1993).

4. *Shock Propagation.*—Since the speeds of shocks are comparable with Alfvénic speeds, with some variation by the Mach number depending on the subsonic or supersonic regime, similar small spatial scales of $l \approx 10^2$–10^3 km would result as determined above for Alfvénic disturbances. Recent models on particle acceleration in shocks produced by reconnection outflows can be found, e.g., in Somov & Kosugi (1997) and Tsuneta & Naito (1998).

5.2. *The Density-Temporal Correlation*

A likely cause of the density-temporal relation $T_{\min} \propto n_e^{-1}$ is a collisional process, because the collisional loss or deflection time has the same reciprocal relation to the electron density of the ambient plasma. Comparing the collisional deflection time (see, e.g., Trubnikov 1965; Spitzer 1967; Schmidt 1979; Benz 1993),

$$T_{\rm Defl}(n_e) = 0.95 \times 10^8\left(\frac{E_{\rm keV}^{3/2}}{n_e}\right)\left(\frac{20}{\ln\Lambda}\right) {\rm s}\,, \tag{35}$$

where $\ln\Lambda$ is the Coulomb logarithm,

$$\ln\Lambda = \ln\left[8.0 \times 10^6 (T_e\, n_e^{-1/2})\right], \quad T_e > 4.2 \times 10^5\ {\rm K}\,, \tag{36}$$

we find for 25 keV electrons an approximate relation (Fig. 9, *right panel*, *dashed curve*),

$$T_{\rm Defl}(n_e,\ E = 25\ {\rm keV}) \approx 0.12\left(\frac{n_e}{10^{11}\ {\rm cm^{-3}}}\right)^{-1} {\rm s^{-1}}\,, \tag{37}$$

that coincides closely with the lower cutoff function of the values $T_{\min}(n_e)$ found from our wavelet analysis (Fig. 9, *right panel*, *squares*).

Comparing the same data with the collisional energy loss time $T_{\rm Loss}$, which is defined by (see, e.g., Trubnikov 1965;

Spitzer 1967)

$$T_{\rm Loss} = 2T_{\rm Defl}\,, \tag{38}$$

we find that most of the minimum wavelet timescales $T_{\rm min}$ still last longer than the collisional loss time $T_{\rm Loss}$ (Fig. 9, *right panel, dotted line*). This observational result implies therefore that the HXR time structures are not produced by the energy loss mechanism itself, which would "erase" all time structures longer than the energy loss time $T_{\rm Loss}$. It is therefore likely that the HXR time structures $T_{\rm min}$ are generated by a modulation mechanism of the acceleration or injection process in a low-density region in the upper corona where the collisional deflection or loss time is longer then the density values n_e measured here, supposedly applying to the loss-cone site where electrons precipitate out of trap regions in flare loops. This result indicates that the acceleration and injection occurs in a low-density region above flare loops, as was also demonstrated by density comparisons of bidirectional (type III + RS) electron beams versus SXR-bright flare loops, where underdensity ratios of $n_e^{\rm acc}/n_e^{\rm SXR} = 0.005$–$0.13$ were inferred for the acceleration site (Aschwanden & Benz 1997).

5.3. *The Peak Timescales $T_{\rm peak}$*

The wavelet scalegrams exhibit power in a continuous range of timescales between the minimum $T_{\rm min} \approx 0.1$–0.7 s and the peak value $T_{\rm peak} \approx 0.5$–128 s. The peak value $T_{\rm peak}$ seems, therefore, to represent an upper cutoff value of a hierarchical range of physical timescales that all play a role in the flare process. The upper cutoff value $T_{\rm peak}$ is likely to be controlled by a macroscopic timescale that encompasses the largest coherently modulated volume of the energy release process (e.g., during a magnetic reconnection or a loop-loop interaction process). The fact that we did not find a correlation between the peak time $T_{\rm peak}$ and the flare loop size r, together with the fact that we found up to three dominant peak timescales per flare, indicates some degree of complexity that a flare is probably made of a superposition of multiple subprocesses.

An interesting idea comes from turbulence theory, in which energy is supplied at the largest spatial scales (and thus largest timescales), which cascades without dissipation over some inertial range down to smaller scales, where it is finally dissipated through viscosity at the smallest scales. It is tempting to apply this turbulence theory to the coronal flare plasma. The upper cutoff or peak timescales $T_{\rm peak}$ could thus be attributed to the macroscopic size of the flare energy release site, where magnetic energy is supplied in form of long-wavelength Alfvénic waves, which is then redistributed via an MHD-turbulent cascade to smaller scales without significant dissipation but is finally dissipated at elementary cells where resistivity is sufficiently high. Such a model has been proposed by LaRosa & Moore (1993). In their scenario, the primary energy source is supplied from magnetic reconnection outflows, which become unstable and turbulent because of the shear viscosity of the plasma, so that the kinetic energy is dissipated in a turbulent cascade. LaRosa & Moore (1993) estimate sizes of $\approx$100–1000 km for the largest turbulent eddies and timescales of $\approx$0.3 s for the resulting HXR spikes, which correspond to our observed minimum timescales of $T_{\rm min} \approx 0.1$–0.7 s. LaRosa, Moore, & Shore (1994) suggest that electrons are also trapped in the large-scale turbulent eddies for about 0.3 s, during which they get accelerated. This trapping mechanism in elementary acceleration cells can explain our observed cutoff of the acceleration time as function of electron density. In summary, an attractive feature of the MHD-turbulent cascade model is the prediction of an inertial range of dissipation timescales, whose power spectrum scales with the wavenumber and can be related to the power-law range $[T_{\rm min}, T_{\rm peak}]$ in our wavelet scalegrams.

Considering energy release in large-scale current sheets as a possible alternative, we note that the obtained size of acceleration cells $r \approx 75$–750 km is of the order of the mean free path of the coronal background plasma, $\lambda_{\rm mfp} \approx 75$ km (at a temperature of 10^7 K and a density of 10^{11} cm^{-3}). The mean free path is just the lower size limit of magnetic island structures that form in metastable current sheets under the action of localized anomalous resistivity, i.e., at the onset of rapid dissipation (Kliem 1995; Schumacher & Kliem 1996). The emerging filamentary current sheet passes through intense dynamical phases of multiple island coalescence and acceleration of the resulting plasmoids, known as the impulsive bursty mode of reconnection (Priest 1985). Substantial electric fields are induced during these processes, which also accelerate particles efficiently in subsecond time intervals (Tajima, Brunel, & Sakai 1982; Kliem 1994; Sakai & de Jager 1996; Schumacher & Kliem 1996). Intermediate timescales are associated with the plasmoids formed by multiple island coalescence in such dynamic current sheets. Hence, these are also consistent with the excitation of a broad range of timescales, as is apparent in the obtained distributions $N(T)$.

In a flare scenario proposed by Somov & Kosugi (1997), a collapsing trap is produced by the downward moving reconnection outflow, which slams into the fast oblique collisionless shock located above the SXR-emitting flare loop. Electrons are energized by first-order Fermi acceleration in the collapsing trap. This scenario is also largely consistent with our observed correlations, because the acceleration time is proportional to the spatial size of the collapsing trap in the cusp region ($T_{\rm min} \propto r$) and the scattering time out of the collapsing trap is related to a collisional timescale. The lifetime of a collapsing trap, which is estimated to $\approx$10 s by Somov & Kosugi (1997), may correspond to the dominant peak time $T_{\rm peak} \approx 0.5$–128 s detected in our wavelet scalegrams.

Besides the maximum timescales of the elementary dissipation processes, some secondary processes can produce a convolution of the elementary timescales and thus lead to large values $T_{\rm peak}$ in our inverted timescale distributions $N(T)$. A well-known secondary process is magnetic trapping of accelerated electrons in the flare loop. The examples described in § 4.4 (Fig. 6) all exhibit large time delays ($\tau = -2.3, \ldots, -7.6$) for high-energy electrons and are thus consistent with collisional trapping times. For these cases, we found a complete lack of fast fine structure up to timescales of $T_{\rm min} > 2.3, \ldots, 5.8$ s. The corresponding peak timescales $T_{\rm peak} = 31$–108 s (in the cases of Fig. 6) are therefore dominated by the convolution with trapping times.

5.4. *Radio Counterparts of Fast HXR Time Structures $T_{\rm min}$*

There are very few other observations that provide potential diagnostics on elementary time and spatial scales in the energy release region of solar flares. The probably best evidence for elementary scales in fragmented energy release sites comes from dynamic spectra of decimetric millisecond spikes (Benz 1985), which show clusters of

$\lesssim 10^4$ elements that correlate in their temporal evolution closely with HXRs (Aschwanden & Güdel 1992). From the frequency bandwidth ($\Delta\nu/\nu \approx 1\%$) of individual spikes, Benz (1986) estimated elementary source sizes of $\Delta h \approx 200$ km, which match well our estimated range, $r_{\rm acc} \approx 75$–750 km. Moreover, the electron density range $n_e \approx 10^9$–10^{12} cm^{-3} (Güdel & Benz 1990) estimated from the plasma frequency of decimetric millisecond spikes agrees well with our density range $n_e \approx 10^{10}$–10^{12} cm^{-3} determined from the energy-dependent delays of the HXR trap component (Aschwanden et al. 1997). From high–time resolution observations (down to 0.5 ms), Güdel & Benz (1990) measured the detailed time profiles of individual spikes and found durations of $T_{\rm radio} \approx 0.02$–$0.10$ s and an exponential decay profile that correlated with the frequency, i.e., $T_{\rm radio}^{\rm decay} \propto \nu^{-1}$, and was thus interpreted in terms of collisional damping, assuming that the observed frequency is in some relation to the plasma frequency, $\nu \approx \nu_p(n_e)$. These radio results bear a remarkable similarity with the findings from our HXR wavelet analysis. Both the decimetric millisecond spikes and the shortest detected HXR pulses have similar durations ($T_{\rm min} \approx 0.1$–0.7 s for HXR spikes), they are detected at similar electron densities, they show a detailed coevolution, and both have decay times that scale reciprocally with the electron density and thus are likely to be attributed to collisional processes. The mutual agreement in all parameters strongly suggests that both the radio and HXR phenomena are associated with the same elementary acceleration processes. We can now exploit complementary information. Decimetric ms spikes appear in clusters of $\lesssim 10^3$–10^4 per major HXR peak ($T \approx 10$–10^2 s), occurring with rates of ≈ 5–100 s^{-1}. This might reveal the true degree of spatial fragmentation. A difference is that the radio spikes, despite their close coevolution with HXRs, exhibit a systematic delay of 2–5 s (Aschwanden & Güdel 1992). However, this delay can be accounted for if the energy of the radio-producing electrons (say ≈ 100 keV) is higher than the ≥ 25 keV HXR-producing electrons and thus can be explained in terms of trapping time differences. The global organization of spike clusters was also investigated by means of symbolic dynamics methods (Schwarz et al. 1993), from which it was concluded that the clustered radio spikes do not represent an ensemble of independently flashing sources but rather are organized by cascades, an interpretation that ties in with the MHD-turbulent cascade model of LaRosa & Moore (1993).

If we use the observed rate ($\Sigma \approx 5$–10^2 s^{-1}) of decimetric millisecond spikes as a measure of the spatial fragmentation of the primary energy release site, which is not too different from the burst rates found in type III–rich flares (e.g., ≈ 10 s^{-1} in the 1980 June 27 flare; Aschwanden et al. 1990), and if we associate the minimum timescale $T_{\rm min}$ as a characteristic acceleration time, we can estimate the total number of electrons accelerated in such elementary cells (with a spatial scale of $l = qr$),

$$\frac{dN_{\rm acc}}{dt} = \frac{An_e\,dV}{T_{\rm min}} = \frac{An_e \sum (qr)^3}{T_{\rm min}}\,, \tag{39}$$

where A denotes the efficiency of the acceleration process. According to the inferred scaling law for Alfvénic waves ($q \approx 0.034$; eq. [34]), we find for typical parameters,

$$\frac{dN_{\rm acc}}{dt} = 4 \times 10^{36} A \left(\frac{n_e}{10^{11}\ {\rm cm}^{-3}}\right)\left(\frac{\sum}{100}\right) \times \left(\frac{r}{10^9\ {\rm cm}}\right)^3 \left(\frac{T_{\rm min}}{0.1\ {\rm s}}\right)^{-1} \text{electrons s}^{-1}\,, \tag{40}$$

This inferred rate of accelerated electrons $dN_{\rm acc}/dt \lesssim 4 \times 10^{36}$ s^{-1} is able to supply the required number of nonthermal ≥ 25 keV electrons up to the largest observed flares (see, e.g., Kane et al. 1983).

6. CONCLUSIONS

We performed for the first time a wavelet analysis of HXR data from solar flares, using high–time resolution data (64 ms) from BATSE/*CGRO* recorded during 647 flare events (1991–1995). We used a wavelet code with triangular wavelets and developed a transformation to convert the obtained scalegrams $S(T)$ into standard distribution functions $N(T)$ of timescales, which have a more direct physical meaning than scalegrams. We performed numerical simulations of time series with single, multiple, periodic, randomly distributed, and multiscale Gaussian time structures, and demonstrated that dominant timescales $T_{\rm peak}$ can be retrieved with an accuracy of ≈ 2 with our scalegram inversion method. We established a significance criterion based on Poisson noise that allows us to quantify the minimum significant timescale $T_{\rm min}$ detected in a wavelet scalegram. Applying this wavelet analysis to 647 solar flares we find the following results:

1. The detected minimum timescales $T_{\rm min}$ cover a very broad time range from the wavelet resolution (128 ms) up to a maximum of $\approx 10^2$ s. In strong flares (with high count rates), the shortest detectable timescales are found in the range $T_{\rm min} \approx 0.1$–0.7 s. In smoothly varying HXR time profiles, which are produced in flares with high trapping efficiency, the shortest detected timescales are found in the range $T_{\rm min} \approx 0.5$–5 s, most likely produced by convolution with trapping timescales. In weak flares, the shortest detected timescales are found to be arbitrarily longer, obviously affected by Poisson noise.

2. The dominant timescales that produce a peak $T_{\rm peak}$ in the timescale distribution $N(T)$ are found to cover a broad range, ≈ 0.5–10^2 s, in different flares. The peak timescale $T_{\rm peak}$ is not correlated with the minimum timescale $T_{\rm min}$. The scalegrams show a continuous distribution of timescales over the range $[T_{\rm min}, T_{\rm peak}]$, with typical power-law slopes of $\beta_{\rm max} \approx 1.5$–$3.2$ (for strong flares), which are compatible with those found for radio bursts in millimeter wavelengths ($\beta \approx 2.2$–2.7; Schwarz et al. 1998).

3. Correlating the minimum timescale $T_{\rm min}$ with the spatial size r of flare loops from *Yohkoh* data, we find a functional dependence $T_{\rm min}(r) \propto r$. Interpreting the timescale $T_{\rm min}$ in terms of an Alfvénic propagation time across an elementary acceleration cell, we obtain sizes of $r_{\rm acc} \approx 75$–750 km, which scale with the flare loop size r, ($r_{\rm acc}/r \approx 3\%$). These spatial scales of elementary acceleration cells agree with those inferred from the frequency bandwidth of decimetric millisecond spikes.

4. The minimum timescale $T_{\rm min}(n_e)$ as function of the electron density n_e exhibits a cutoff that coincides roughly with the collisional deflection time $T_{\rm Defl}(n_e)$ for ≥ 25 keV electrons at the loss-cone site of flare loops.

While this study represents only a first step in the exploration of wavelet analysis applied to solar flare HXR emis-

sion, a lot of tasks are left for future work. One aspect that has not been addressed in our wavelet analysis is the stationarity. In principle, the flare processes manifested during the 4 minute intervals analyzed here could be nonstationary and intermittent, requiring a subdivision into stationary intervals (Isliker & Kurths 1993; Kurths & Schwarz 1994; Isliker & Benz 1994). A more detailed modeling is necessary to interpret our findings. The identification of stationary intervals might provide more accurate scalegrams and inverted timescale distributions $N(T)$. Also, a detailed theoretical study on scalegram properties as function of elementary time profiles is the subject of a subsequent study (Kliem et al. 1998).

We thank Ph. Bendjoya and J. M. Petit for providing the wavelet code. We thank the BATSE principal investigator, Jerry Fishman, for generous release of the BATSE data and the MSFC and the GSFC Solar Data Analysis Center (SDAC) for archiving and computational ressources. We are grateful for helpful comments by Arnold Benz, Stephen White, and an anonymous referee. The work of M. J. A. was partially supported by NASA SR&T grant NAG-5-5078/ NAG5-4026 and *CGRO* grant NAG5-3593. The work of B. K. was supported by DARA grant 01-OC-9706 and by grant 28-3381-1/57(97) of the MWFK Brandenburg. J. K. and U. S. were partly supported by a DAAD grant.

REFERENCES

Alexander, D., & Metcalf, T. 1997, ApJ, 489, 442
Aschwanden, M. J., & Benz, A. O. 1997, ApJ, 1997, ApJ, 480, 825
Aschwanden, M. J., Benz, A. O., Dennis, B. R., & Kundu, M. R. 1994a, ApJS, 90, 631
Aschwanden, M. J., Benz, A. O., Dennis, B. R., & Schwartz, R. A. 1995a, ApJ, 455, 347
Aschwanden, M. J., Benz, A. O., & Montello, M. 1994b, ApJ, 431, 432
Aschwanden, M. J., Benz, A. O., & Schwartz, R. A. 1993, ApJ, 417, 790
Aschwanden, M. J., Benz, A. O., Schwartz, R. A., Lin, P. R., Pelling, R. M., Stehling, W. 1990, Sol. Phys., 130, 39
Aschwanden, M. J., Bynum, R. M., Kosugi, T., Hudson, H. S., & Schwartz, R. A. 1997, ApJ, 487, 936
Aschwanden, M. J., Dennis, B. R., & Benz, A. O. 1998a, ApJ, 497, 972
Aschwanden, M. J., & Güdel, M. 1992, ApJ, 401, 736
Aschwanden, M. J., Hudson, H. S., Kosugi, T., & Schwartz, R. A. 1996a, ApJ, 464, 985
Aschwanden, M. J., Kosugi, T., Hudson, H. S., Wills, M. J., & Schwartz, R. A. 1996b, ApJ, 470, 1198
Aschwanden, M. J., & Schwartz, R. A. 1995, ApJ, 455, 699
Aschwanden, M. J., Schwartz, R. A., & Alt, D. M. 1995b, ApJ, 447, 923
Aschwanden, M. J., Schwartz, R. A., & Dennis, B. R. 1998b, ApJ, 502, 468
Aschwanden, M. J., Wills, M. J., Hudson, H. S., Kosugi, T., & Schwartz, R. A. 1996c, ApJ, 468, 398
Bendjoya, Ph., Petit, J.-M., & Spahn, F. 1993, Icarus, 105, 385
Benz, A. O. 1993, Plasma Astrophysics, Kinetic Processes in Solar and Stellar Coronae (Dordrecht: Kluwer)
———. 1985, Sol. Phys., 96, 357
———. 1986, Sol. Phys., 104, 99
Bocchialini, K., & Baudin, F. 1995, A&A, 299, 893
Cliver, E. W., Hurst, M. D., Wefer, F. L., Bleiweiss, M. P. 1976, Sol. Phys., 48, 307
Damiani, F., Maggio, A., Micela, G., & Sciortino, S. 1997a, ApJ, 483, 350
———. 1997b, ApJ, 483, 370
Daubechies, I. 1992, Ten Lectures on Wavelets (Philadelphia: Soc. Industrial Appl. Math.)
DeJager, C., & DeJonge, G. 1978, Sol. Phys., 58, 127
Dennis, B. R., Benz, A. O., Ranieri, M., & Simnett, G. M. 1984, Sol. Phys., 90, 383
Doschek, G. A., Strong, K. T., & Tsuneta, S. 1995, ApJ, 440, 370
Emslie, A. G. 1983, ApJ, 271, 367
Fishman, G. J., et al. 1989, in Proc. *GRO* Science Workshop, ed. W. N. Johnson (Greenbelt: GSFC), 2
Frick, P., Baliunas, S. L., Galyagin, D., Sokoloff, D., & Soon, W. 1997, ApJ, 483, 426
Fröhlich, C., et al. 1997, Sol. Phys., 170, 1
Güdel, M., & Benz, A. O. 1990, A&A, 231, 202
Hudson, H. S. 1994, in AIP Conf. Proc. 294, High-Energy Solar Phenomena—A New Era of Spacecraft Measurements, ed. J. Ryan & W. T. Vestrand (New York: AIP), 151
Hudson, H. S., & Ryan, J. 1995, ARA&A, 33, 239
Isliker, H, & Benz, A. O. 1994, A&A, 285, 663
Isliker, H., & Kurths, J. 1993, Int. J. Bifurcation and Chaos, 3(6), 1573
Kane, S. R., Kai, K., Kosugi, T., Enome, S., Landecker, P. B., & McKenzie, D. L. 1983, ApJ, 271, 376
Kiplinger, A., Dennis, B. R., Emslie, A. G., Frost, K. J., & Orwig, L. E. 1983a, ApJ, 265, L99
Kiplinger, A., Dennis, B. R., Frost, K. J., & Orwig, L. E. 1982, in Proc. Hinotori Symposium on Solar Flares (Tokyo: Instit. Space Astronaut. Sci.), 66
———. 1983b, ApJ, 273, 783
Kliem, B. 1994, ApJS, 90, 719
———. 1995, in Lecture Notes in Physics 444, Coronal Magnetic Energy Releases, ed. A. O. Benz & A. Krüger (Berlin: Springer), 93
Kliem, B., et al. 1998, in preparation
Komm, R. W. 1994, in ASP Conf. Proc. 68, Solar Active Region Evolution: Comparing Models with Observations, eds. K. S. Balasubramaniam & G. W. Simon (San Francisco: ASP), 24
———. 1995, Sol. Phys., 157, 45
Kurths, J., Benz, A. O., & Aschwanden, M. J. 1991, A&A, 248, 270
Kurths, J., & Herzel, H. 1986, Sol. Phys., 107, 39
———. 1987, Physica, 25D, 165
Kurths, J., & Karlicky, M. 1989, Sol. Phys., 119, 399
Kurths, J., & Schwarz, U. 1994, Space Sci. Rev., 68, 171
Kurths, J., Schwarz, U., & Witt, A. 1995, in Lecture Notes in Physics 444, Coronal Magnetic Energy Releases, ed. A. O. Benz & A. Krüger (Berlin: Springer),159
LaRosa, T. N., & Moore, R. L. 1993, ApJ, 418, 912
LaRosa, T. N., Moore, R. L., & Shore, S. N. 1994, ApJ, 425, 856
Machado, M. E., Ong, K. K., Emslie, A. G., Fishman, G. J., Meegan, C., Wilson, R., & Paciesas, W. S. 1993, Adv. Space Res., 13(9), 175
Mallat, S. G. 1989, IEEE Trans. Pattern Anal. Machine Intelligence, 11, 674
Mangeney, A., & Pick, M. 1989, A&A, 224, 242
Masuda, S. 1994, Ph.D. thesis, Univ. Tokyo
Masuda, S., Kosugi. T., Hara, H., Sakao, T., Shibata, K., & Tsuneta, S. 1995, PASJ, 47, 677
Masuda, S., Kosugi, T., Hara, H., Tsuneta, S., & Ogawara, Y. 1994, Nature, 371, 49
Meyer, Y., & Ryan, R. D. 1993, Wavelets: Algorithms and Applications (Philadephia: Soc. Indust. Appl. Math.)
Orwig, L. E., Frost, K. J., & Dennis, B. R. 1980, Sol. Phys., 65, 25
Parks, G. K., & Winckler, J. R. 1969, ApJ, 155, L117
Priest, E. R. 1985, Rep. Prog. Phys., 48, 955
Ryabov, V. B., Stepanov, A. V., Usik, P. V., Vavriv, D. M., Vinogradov, V. V., & Yurovsky, Y. F. 1997, A&A, 324, 750
Sakai, J.-I., & de Jager, C. 1996, Space Sci. Rev., 77,1
Scargle, J. D. 1993, in Applications of Time Series Analysis in Astronomy and Meteorology, ed. T. Subba Rao, M. B. Priestley, O. Lessi, & E. J. Hannan (London: Chapman & Hall)
Scargle, J. D., Steiman-Cameron, T., Young, K., Donoho, D. L., Crutchfield, J. P., & Imamura, J. 1993, ApJ, 411, L91
Schmidt, G. 1979, Physics of High Temperature Plasmas (2d ed.; New York: Academic)
Schumacher, J., & Kliem, B. 1996, Phys. Plasmas, 3, 4703
Schwarz, U., Benz, A. O., Kurths, J., & Witt, A. 1993, A&A, 277, 215
Schwarz, U., Kurths, J., Kliem, B., Krüger, A., & Urpo, S. 1998, Ap&SS, 127, 309
Shibata, K., Masuda, S., Shimojo, M., Hara, H., Yokoyama, T., Tsuneta, S., Kosugi, T., & Ogawara, Y. 1995, ApJ, 451, L83
Somov, B. V., & Kosugi, T. 1997, ApJ, 485, 859
Spitzer, L. 1967, The Physics of Fully Ionized Gases (2d ed.; New York: Interscience)
Tajima, T., Brunel, F., & Sakai J. 1982, ApJ, 258, L45
Takakura, T., Inda, M., Makishima, K., Kosugi, T., Sakao, T., Masuda, S., Sakurai, T., & Ogawara, Y. 1993, PASJ, 45, 737
Trottet, G., Kerdraon, A., Benz, A. O., & Treumann, R. 1981, A&A, 93, 129
Trubnikov, B. A. 1965, Rev. Plasma Physics, 1, 105
Tsuneta, S. 1995, PASJ, 47, 691
———. 1996, ApJ, 456, 840
Tsuneta, S., & Naito, T. 1998, ApJ, 495, L67
Vigoroux, A., & Delache, Ph. 1993, A&A, 278, 607
Wang, H., Gary, D. E., Zirin, H., Kosugi, T., Schwartz, R. A., & Linford, G. 1995, ApJ, 444, L115
Watari, S. 1995, Sol. Phys., 158, 365
———. 1996, Sol. Phys., 163, 371
Wheatland, M. S., & Melrose, D. B. 1995, Sol. Phys., 158, 283
Young, C. A., Meredith, D. C., & Ryan, J. M. 1995, Ap&SS, 231, 119
Zhao, R. Y., Mangeney, A., & Pick, M. 1991, A&A, 241, 183